Computers and Concrete, *Vol. 38, No. 1 (2026) 157-191*
https://doi.org/10.12989/cac.2026.38.1.157

Predicting the axial load capacity of circular concrete-filled steel tube columns confined with fiber-reinforced polymer using machine learning models

Sema Alacali[1a], Fatih Cibuk*[2]

[1]*Department of Civil Engineering, Yildiz Technical University, Istanbul, Türkiye*
[2]*Department of Civil Engineering, Istanbul Medipol University, Istanbul, Türkiye*

(Received March 9, 2026, Revised May 9, 2026, Accepted June 9, 2026)

Abstract. In this study, a new model was developed to predict the axial load-carrying capacity of circular concrete-filled steel tube (CFST) columns externally confined with fiber-reinforced polymer (FRP). For this purpose, 227 experimental data points collected from the literature were split, with 75% for training and 25% for testing. A new equation was then derived using Gene Expression Programming (GEP). Additionally, prediction models were developed using several machine learning (ML) algorithms, including MLP (Multilayer Perceptron), KNN (K-Nearest Neighbors), BAG (Bootstrap Aggregating), RF (Random Forest), GBM (Gradient Boosting Machine), LightGBM (Light Gradient Boosting Machine), XGBoost (Extreme Gradient Boosting), and CatBoost (Categorical Boosting). A 10-fold cross-validation approach was employed during the grid search to identify the optimal hyperparameter combination for the ML models. The predictive performances of the proposed models were statistically evaluated and compared with existing equations in the literature. CatBoost demonstrated the best predictive performance on the test data, with a MAPE of 4.075, an RMSE of 180.509, an R^2 of 0.988, and a COV of 0.059. SHAP analysis was used to evaluate the contribution of each input parameter to the prediction results.

Keywords: concrete-filled steel tube (CFST) columns; fiber-reinforced polymer (FRP); gene expression programming (GEP); machine learning (ML)

1. Introduction

Composite structural elements, which are formed by combining concrete and steel materials, are widely used today. One of these composite elements, circular section concrete-filled steel tube columns, is frequently preferred in building systems. The confining effect of the steel tube on the concrete core and the prevention of buckling of the steel tube by the concrete core significantly increase the strength and ductility of the column element [1]. The experiments showed that the typical failure mode of concrete-filled steel tube columns is outward local buckling [2]. The fiber-reinforced polymer confined around the outer surface of the steel tube delays the outward local buckling that may occur and prevents the sudden strength reduction caused by local buckling in the steel tube [2-4]. Fiber reinforced polymers are composite materials that have been frequently

*Corresponding author, Research Assistant, Ph.D. Candidate, E-mail: fatih.cibuk@medipol.edu.tr
[a] Associate Professor, E-mail: noyan@yildiz.edu.tr

http://www.techno-press.org/cac/5 ISSN: 1598-8198 (Print), 1598-818X (Online)

used in construction projects and research papers over the past decade. Carbon, glass and basalt fibers are among the most commonly used materials in FRP production. Although they are more costly than traditional building materials such as steel, their light weight, corrosion resistance and high strength make FRPs a preferred option for many applications [5-8].

Numerous studies in the literature have investigated the behavior of Fiber Reinforced Polymer (FRP)-confined Concrete-Filled Steel Tube (CFST) columns. Research indicates that an increase in the number of FRP layers significantly enhances the load-carrying capacity and ductility of circular CFST columns [9-13]. While the efficiency of FRP confinement increases proportionally with the number of layers, it has been observed that this efficiency decreases as concrete strength increases [3]. Cross-sectional geometry and fiber type are decisive factors in the effectiveness of the confinement; while CFRP confinement significantly increases the load-carrying capacity in circular columns, this effect remains limited in rectangular columns [10]. Furthermore, the confinement effect provided by CFRP diminishes as the slenderness ratio of the column increases [11]. When comparing fiber types, it has been found that CFRP contributes more to strain and ultimate strength than GFRP, whereas GFRP provides superior ductility [13]. The use of FRP offers a vital advantage by delaying or preventing local buckling in the steel tube, thereby enhancing mechanical life and resistance [14]. Additionally, CFRP confinement is considered an effective method for restoring the load-carrying capacity, stiffness, and ductility of CFST columns damaged by high temperatures [15].

So far, numerous analytical and numerical models as well as experimental studies have been introduced to predict the load carrying capacity of CFST columns with circular cross-section confined with FRP under axial loading. In addition to models derived by traditional methods, recent studies indicate that the predictions obtained by using machine learning (ML) algorithms provide significant advantages in terms of accuracy and performance. ML models are a rapidly developing subfield of artificial intelligence used to generate and evaluate high-performance predictions in engineering applications. At the same time, ML models have the technology to analyze the identified data, establish relationships between them, and evaluate these relationships.

Recently, in the field of structural engineering, machine learning (ML) algorithms have been used to predict the load-bearing capacities of structural elements on various research manners such as moment capacity of ferrocement elements [16], punching shear capacity of RC slab-column connections with FRP bars [17], plastic hinge length of rectangular RC columns [18], shear strength of steel fiber reinforced concrete [19] and moment redistribution capacity in reinforced concrete beams [20]. Alacali et al. developed a model based on GEP to predict the shear strength of FRP-reinforced beams. In this study, separate prediction models were developed for three different reinforcement configurations, namely, fully confined, U-confined and side bonded, and it was shown that these models exhibited statistically higher performance compared to the models proposed in current regulations and other researchers [21]. Ye et al. evaluated the performance of numerous ML models for predicting the shear strength of ultra-high-performance concrete (UHPC) beams. The results show that the CatBoost model exhibits higher prediction performance compared to the other algorithms [22]. Almasabha et al. assembled a dataset comprising 102 synthetic fiber-reinforced concrete beam samples from existing studies to examine the shear strength of these beams. They employed various ML models to predict shear strength. Additionally, they compared the performance of these methods against the ACI 318-19 equation. The findings revealed that LightGBM achieved the highest prediction accuracy, whereas the ACI 318-19 equation showed the lowest predictive accuracy [23]. Zareian et al. developed several ML models to predict the seismic response of moment-resisting steel frames. The results of the study reveal that LightGBM and CatBoost models show superior prediction performance [24].

With the widespread use of ML models in different engineering fields, numerous studies have also been conducted on CFST columns, which are the focus of this study, to predict their load-carrying capacity. Güneyisi et al. developed a model using GEP to predict the axial load-carrying capacity of circular-section CFST columns [25]. Tran et al. obtained a relationship for predicting the axial compressive capacity using the ANN method, based on experimental data of circular-section CFST columns collected from the literature and a database created in the finite element model [26-27]. Zarringol et al. derived separate relationships for axially and eccentrically loaded column groups by using ANN considering a test data set of CFST columns with rectangular and circular sections [28]. Vu et al. evaluated the performance of several ML models and compared their predictive capabilities [29]. Naser et al. proposed separate equations for estimating the load-carrying capacity of CFST columns with circular and rectangular sections subjected to axial or eccentric loading using genetic algorithm (GA) and GEP [30]. Hou and Zhou compared the performance of several ML models in predicting the axial compressive strength of CFST columns and evaluated their prediction results [31]. Güneyisi et al. derived a relation for the prediction of axial load carrying capacity using 92 circular section CFST column specimens confined with carbon or glass fiber with length/diameter ratio ranging from 2.0 to 4.5. GEP was used during the relation derivation process [32]. Miao et al. employed ML models to predict the ultimate strength of FRP-confined circular CFST columns [33].

This study differs from previous research in several key aspects. First, the dataset used is among the most comprehensive in terms of the number of experiments compiled from the literature, consisting of 227 CFST short columns subjected to monotonic loading. This enables the models to capture a wider range of parameter variations and improves their generalization capability. In addition, rather than focusing on a limited number of approaches, multiple machine learning models were evaluated and compared within a consistent framework. To assess model performance, the predictions obtained from existing empirical equations, various machine learning algorithms, and the newly developed GEP formulation were systematically compared using statistical metrics. The results show that the GEP model achieves higher prediction accuracy than the others. Furthermore, unlike traditional empirical equations that are typically restricted to narrow parameter ranges, the proposed approach provides a more flexible and generalized solution, maintaining its accuracy over a broader range of design conditions.

In this context, despite existing studies, a comprehensive comparison of advanced ML models for predicting the axial load-carrying capacity of CFST short columns remains limited. Therefore, in this study, several ML-based prediction models were developed using a dataset compiled from the literature. The predictive performances of these models, together with the equations proposed in previous studies, were statistically compared. The results indicate that the CatBoost model provides the most accurate predictions. Furthermore, feature importance analysis was applied to interpret the behavior and effectiveness of the proposed model.

2. Summary of experimental data

In this study, a dataset comprising the experimental results of 227 FRP confined CFST columns, tested by 24 different researchers in the literature, was utilized. The dataset presented in Table 1, includes the following parameters: the diameter of the steel tube (D), the thickness of the steel tube (t_s), the thickness of the FRP (t_f), the tensile strength of the FRP (f_f), the modulus of

Table 1. Descriptive statistics of the variables

Variable	Mean	Standard deviation	Median	Minimum	Maximum
D (mm)	174.14	64.73	139.80	100	305
t_s (mm)	3.25	1.50	3	1	7.50
t_f (mm)	0.40	0.45	0.33	0.11	3
f_f (MPa)	3368.07	916.02	3481	770	4900
E_f (GPa)	206.64	67.04	235	19	257
L (mm)	503.81	224.46	402.50	200	1500
f_y (MPa)	302.42	42.50	299	226	369
f_c' (MPa)	44.09	17.95	43.20	14.33	112.24
N_u (kN)	2698.38	1601.89	2063	591	7407

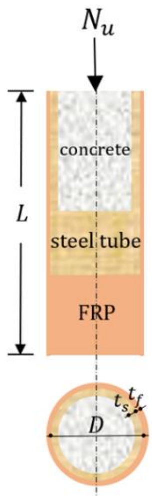

Figure 1. The schematic representation of fiber-reinforced polymer confined CFST columns

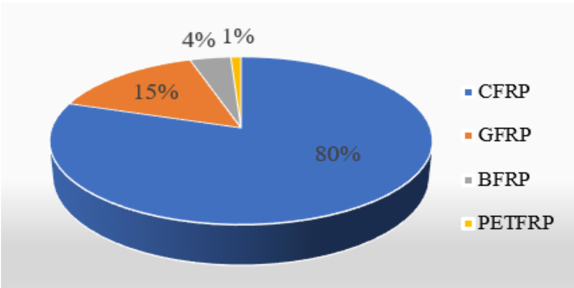

Figure 2. Distribution of test specimens by FRP type

elasticity of the FRP material (E_f), the length of the steel tube (L), the yield strength of the steel tube (f_y), the compressive strength of the cylinder concrete (f_c') and the axial load carrying capacity (N_u). The detailed dataset is provided in Appendix Table A1, while the descriptive statistics of the variables are summarized in Table 1.

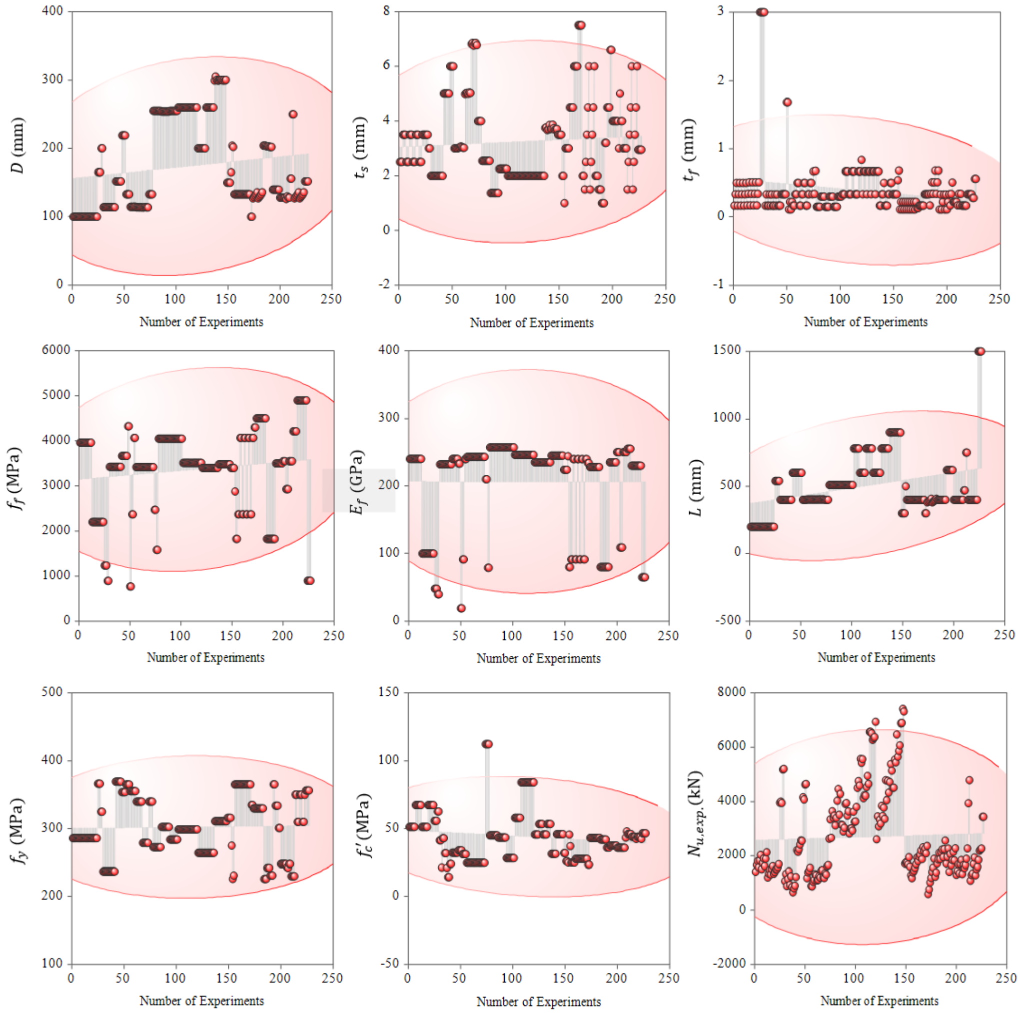

Figure 3. Scatter plots of the variables considered in the analysis

Fig. 1 illustrates the schematic representation of the geometrical parameters of the columns. Fig. 2 also depicts the types of FRP and proportions of the test specimens. As shown in Fig. 2, the experimental dataset complied from the literature consists of 227 data points, including 182 CFRP (Carbon Fiber Reinforced Polymers 80%), 33 GFRP (Glass Fiber Reinforced Polymers 15%), 10 BFRP (Basalt Fiber Reinforced Polymers 4%), and 2 PETFRP (Polyethylene Terephthalate Fiber Reinforced Polymers 1%) type polymers.

The compressive strength of the concrete filling was determined through tests on cylindrical and cubic specimens. To ensure consistency and reliability in the analysis, the concrete compressive strengths need to be converted to a common measurement unit. In this study, the cube compressive strengths were converted to cylindrical compressive strengths using Eq. (1), as proposed by Goode and Lam [34], following the Chinese Standard (GB 50010). In this context, f_{cu} and f_c' represent the cube and cylindrical compressive strengths of concrete, respectively.

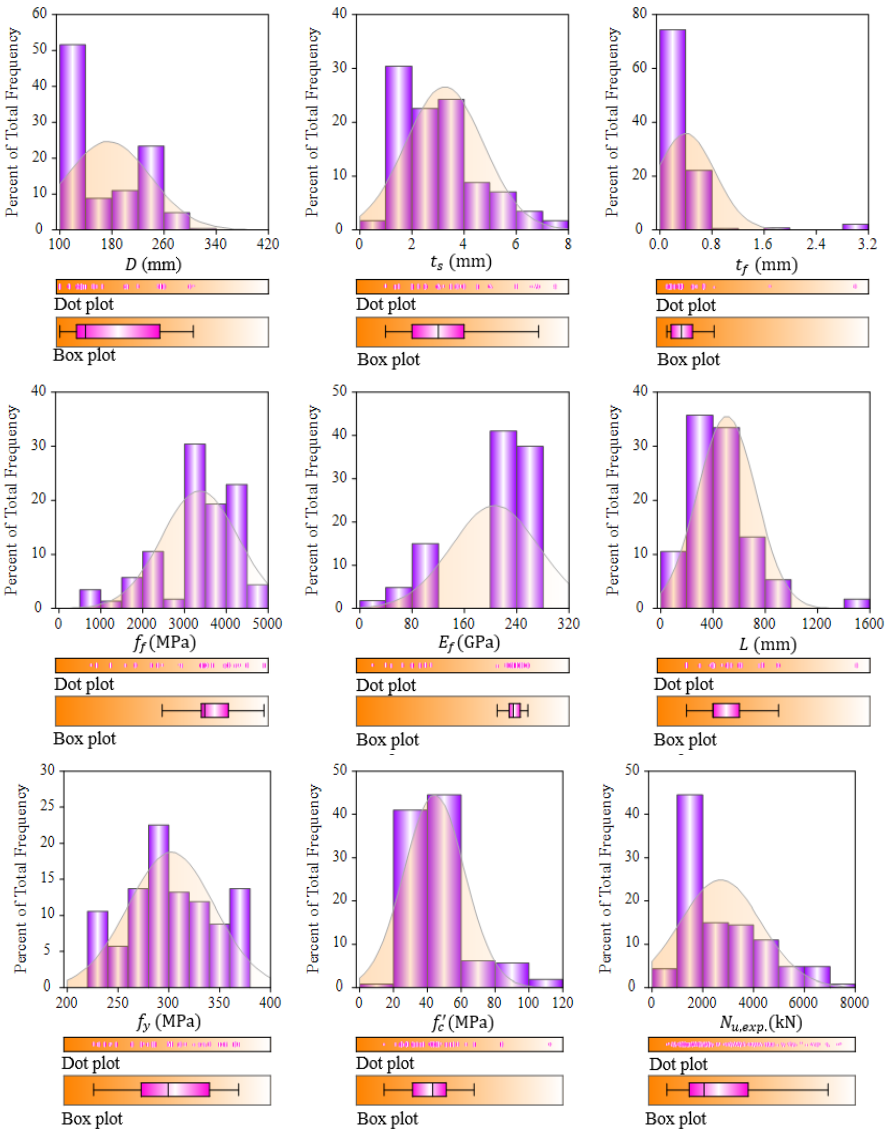

Figure 4. Frequency distributions of the variables

$$f_c' = 0.8 f_{cu} \tag{1}$$

Fig. 3 presents the scatter plots for each variable considered in the analysis.

Furthermore, Fig. 4 illustrates the histogram, dot plot, and box plot distributions of the variables, where the vertical axis represents the percent of total frequency.

The Pearson correlation coefficients, which illustrates the strength of the linear relationships between the variables in the dataset and ranges from -1 and +1, is presented in Fig. 5. A positive correlation coefficient indicates a linear relationship between two variables in the same direction, whereas a negative correlation coefficient signifies a linear relationship in the opposite direction.

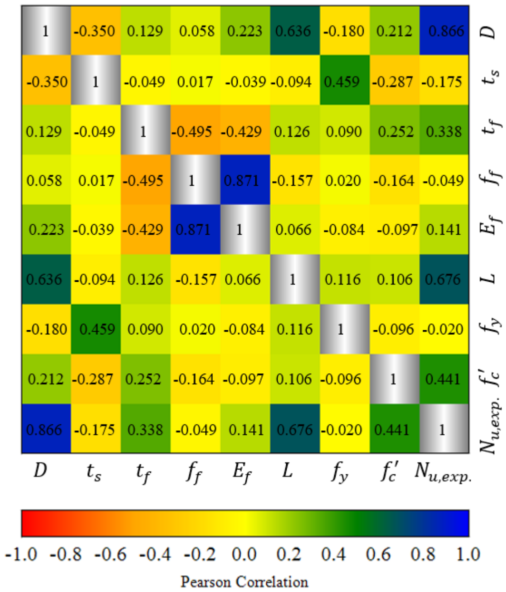

Figure 5. Pearson correlation coefficients of the variables

Based on the correlation results, the variables with the strongest effect on the axial load-carrying capacity were identified as D and L. Specifically, D (0.866) showed a very strong positive correlation, significantly increasing the carrying capacity, while L (0.676) also exhibited a strong positive relationship. Among the variables with medium level effect, f_c' (0.441) and t_f (0.338) were identified, providing limited but positive contributions. E_f (0.141) demonstrated a low-level positive effect on the carrying capacity. Among the variables with a negative correlation, t_s (-0.175) had a slightly reducing impact on the carrying capacity. In contrast, f_f (-0.049) and f_y (-0.020) exhibited negligible effects. Consequently, D and L emerge as the critical variables influencing the carrying capacity, whereas the effects of other variables are either limited or insignificant. Nonetheless, in this study, all variables were considered to comprehensively evaluate the interactions between variables and to understand the contribution of each factor to the carrying capacity in a more comprehensive manner.

3. Review of existing formulations for FRP-confined CFST columns under axial compression

The equations proposed by various researchers in the literature for predicting the axial load-carrying capacity of circular CFST columns confined with FRP are presented in this section. In these equations, A_s represents the cross-sectional area of the steel tube, A_c denotes the cross-sectional area of the concrete core, A_t denotes the total cross-sectional area of the concrete and steel tube and A_f refers to the cross-sectional area of the FRP jacket. Additionally, ξ_s and ξ_f represent the confinement factors for the CFST and the FRP jacket, respectively. The confinement factors ξ_s and ξ_f are determined using Eqs. (2) and (3):

Table 2. Recommended coefficient "c" based on FRP type

FRP Type	Number of layers		
	1 layer	2 layers	3 layers
BFRP	1.59	1.25	1.01
CFRP	1.23	0.94	0.83

$$\xi_s = \frac{A_s f_s}{A_c f_c'}, \tag{2}$$

$$\xi_f = \frac{A_f f_f}{A_c f_c'}. \tag{3}$$

3.1 Liu et al. [35]

Liu et al. experimentally and theoretically investigated the buckling behavior of FRP-confined CFST columns under axial compression after exposure to a corrosive environment. They also proposed the equation presented in Eq. (4) to predict the axial load-carrying capacity of circular CFST columns confined with CFRP and BFRP. The coefficient "c" in Eq. (4) is obtained from Table 2, which provides values for columns confined with CFRP and BFRP in different layer configurations [35].

$$N_u = \left(1 + 1.40\xi_s + c\xi_f\right) f_c' A_c \tag{4}$$

3.2 Tang et al. [12]

Tang et al. investigated the behavior of concrete-filled stainless-steel tube (CFSST) columns reinforced with FRP under axial loading. The failure mechanisms and load-displacement curves of 18 columns confined with CFRP were obtained. As a result of their investigation, they proposed Eq. (5) to predict the axial load carrying capacity of these columns [12].

$$N_u = (1 + \eta_{cap})(1.27 F A_s + 0.85 f_c' A_c) \tag{5}$$

The parameters F and η_{cap} in this equation are defined in Eqs. (6) and (7):

$$F = \min\,(f_y; 0.7 f_u), \tag{6}$$

$$\eta_{cap} = 0.42\,\frac{\xi_f}{\xi_s}. \tag{7}$$

3.3 Ding et al. [36]

Ding et al. conducted an experimental and theoretical study on CFST columns confined with CFRP. They investigated the effects of varying CFRP layer numbers and concrete strengths on the mechanical performance of the columns. As a result of their study, the equation presented in Eq. (8) was proposed to predict the axial load-carrying capacity [36].

$$N_u = 0.4\left(1 + 1.7\xi_s + 1.7\xi_f\right)A_c f_{cu}^{7/6} \tag{8}$$

3.4 Lu et al. [37]

Lu et al. developed Eqs. (9) and (10) to predict the axial load-carrying capacity of CFST columns confined with CFRP and GFRP. When determining the axial load-carrying capacity of the column, Eq. (9) is recommended when the confinement factor ξ_s is less than 1.235, whereas Eq. (10) is used when ξ_s exceeds this threshold [37].

$$N_u = \left(1 + 2\xi_s + 1.36\xi_f\right)A_c f_c', 0 \le \xi_s \le 1.235 \tag{9}$$

$$N_u = \left(1 + 1.1\xi_s + \sqrt{\xi_s} + 1.36\xi_f\right)A_c f_c', \xi_s > 1.235 \tag{10}$$

3.5 Lu et al. [3]

Lu et al. conducted tested on 11 columns to examine the effects of the number of FRP layers, steel tube thickness, and concrete strength on load capacity and axial deformation. They also proposed the model presented in Eq. (11) to predict the axial load carrying capacity [3].

$$N_u = \left(1 + 1.8\xi_s + 1.15\xi_f\right)A_s f_c' \tag{11}$$

3.6 Wei et al. [4]

Wei et al. conducted an experimental study to investigate the effects of steel tube thickness, FRP type and number of layers on the axial compressive load carrying capacity of CFST columns confined with carbon and basalt fiber reinforced polymer (FRP). He also developed the model given in Eq. (12) to predict the axial load-carrying capacity by utilizing studies from the literature [38-39].

$$N_u = A_t\left(1 + 1.27\xi_s + 1.28\xi_f\right)f_c' \tag{12}$$

3.7 Che et al. [1]

Che et al. investigated the load carrying capacity, stiffness variations and load-deformation behavior of circular CFST columns confined with CFRP through both experimental testing and ABAQUS finite element modeling. Based on their analysis, they proposed the model presented in Eq. (13) to predict the axial load carrying capacity [1].

$$N_u = 0.67\left(1.14 + 1.02\left(\xi_s + 3\xi_f\right)\right)A_t f_{cu} \tag{13}$$

3.8 Tao et al. [10]

Based on the equations proposed by Han et al. [40] for predicting the load-carrying capacity of circular CFST columns and by Yu et al. [41] for predicting the load-carrying capacity of CFRP-

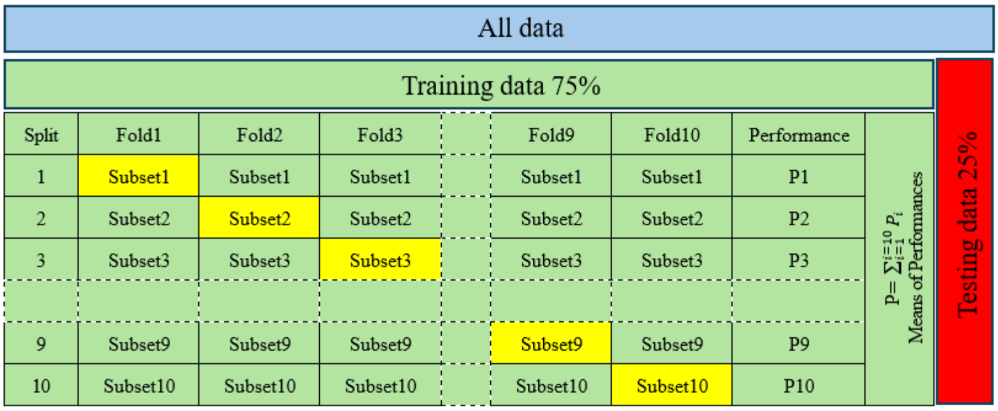

Figure 6. 10-fold cross validation

confined concrete specimens, Tao et al. derived Eq. (14) to predict the load-carrying capacity of CFRP-confined circular CFST columns [10].

$$N_u = (1 + 1.02\xi_s)f_c' A_t + 1.15\xi_f f_c' A_c \tag{14}$$

4. Overview of machine learning methods

Models have been developed in this study using algorithms with GEP, MLP, KNN, BAG, RF, GBM, LightGBM, XGBoost, and CatBoost for predicting the load carrying capacity of the columns. For all models, the dataset used, consisting of eight input parameters, and one output parameter was passed through random shuffling and splitting into 75% training data and 25% testing data used in all ML models.

This approach was used to assess the generalizability of the model and reduce the risk of overfitting. For the GEP model, a predictive model was developed using GeneXproTools 5.0, and an equation was formulated.

In other ML models, the Python programming language was utilized within the Jupyter library of Anaconda software. StandardScaler, a data preprocessing tool from Python's scikit-learn library, was applied to scale all parameters in the dataset to improve the performance of ML models and achieve faster convergence. StandardScaler standardizes each parameter by transforming it to have a mean of zero and a standard deviation of one, as defined by Eq. (15):

$$z = \frac{x-m}{\sigma}. \tag{15}$$

Regressor models were imported from the scikit-learn Python libraries. In the ML models, grid search and 10-fold cross-validation method were applied to the training set for hyperparameter tuning and to assess the predictive ability of each model. As illustrated in Fig. 6, the training set was split into ten subsets, where the model was on nine subsets, and the remaining subset was used for validation. This process is repeated ten times, ensuring that each subset served as the validation set once. Finally, the mean value of the prediction results from ten training cycles was used to increase reliability by reducing the variance associated with a single training-testing split.

Table 3. Optimal hyperparameters for ML models

Model	Details of hyperparameters	
GEP	Input parameters	D (mm), t_s (mm), t_f (mm), f_f (MPa), E_f (GPa), L (mm), f_y (MPa), f_c'(MPa)
	Output parameter	N_u (kN)
	Training set (%75)	170
	Testing set (%25)	57
	Chromosomes	150
	Head Size	8
	Genes	8
	Linking function between ETs	Addition
	Constants per gene	10
	Function set	$+. -. \times. \div. \sqrt{.}. x^2. x^3. x^{1/4}.$ sin. tan
	Mutation	0.00138
	Inversion rate	0.00546
	One-Point Recombination	0.3
	Two-Point Recombination	0.3
	Gene Recombination	0.1
MLP	activation=relu, alpha=0.005, hidden_layer_sizes=(400, 300, 200)	
KNN	neighbors=5	
BAG	n_estimators=72	
RF	max_depth=15, max_features=5, n_estimators=250	
GBM	learning_rate=0.1, max_depth=3, n_estimators=200, subsample=0.50	
LightGBM	learning_rate=0.5, max depth=2, n_estimators=200, colsample_bytree=0.9,	
XGBoost	colsample_bytree=1, learning_rate=0.1, max_depth=2, n_estimators=1000	
CatBoost	iterations=2000, learning_rate=0.05, depth=3	

Using a variety of algorithms and methods, ML models aim to uncover hidden relationships in data by learning patterns and making predictions, thereby accurately predicting target variables. The performance of different models may vary depending on the structure of the data and the type of problem. The ML models employed to obtain the most accurate predictive model will be briefly introduced in the following section. The optimal hyperparameters utilized in each ML model are presented in Table 3.

4.1 Gene expression programming

Gene Expression Programming (GEP) is a ML model designed to identify relationships between variables in datasets and construct models that represent these relationships. The GEP model development process starts with the random generation of chromosomes within the dataset population defined in the program. The suitability of these randomly generated chromosomes is evaluated, and new offspring with modified characteristics are introduced through genetic operations. New generations of chromosomes undergo the same evolutionary process, which is

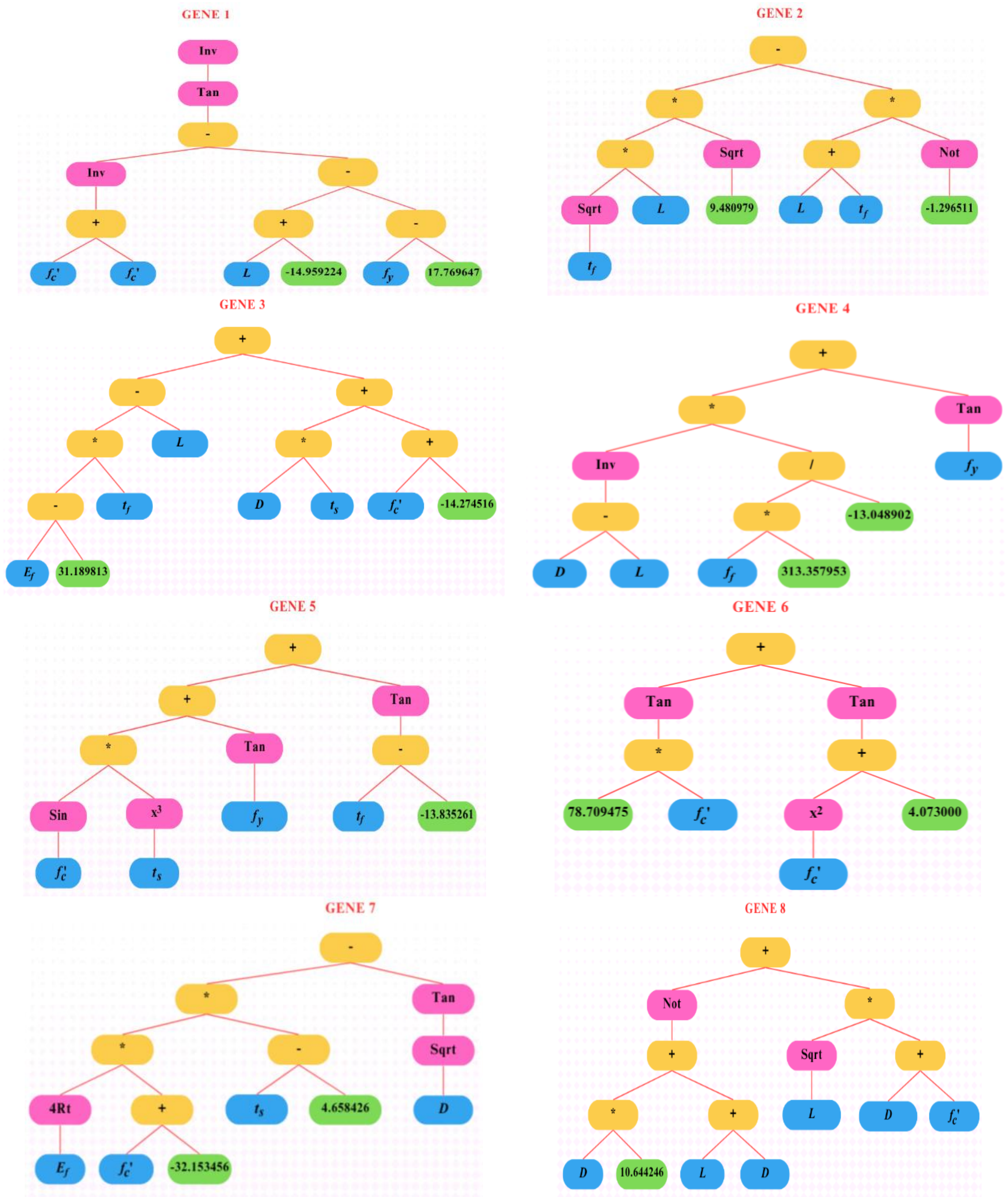

Figure 7. Expression trees (ETs) of GEP model for N_u

repeated until an optimal solution is obtained.

Reproduction in chromosomes not only enables the replication and transmission of genes to the next generation but also incorporates genetic operators that introduce genetic variation [42]. If the range of application of genetic operators used in deriving relationships via GEP is too narrow, populations evolve very slowly and may not reach an optimal solution. Conversely, if the range of application is excessively wide, a large number of solutions far from the desired fitness are obtained [43]. To improve the solutions of complex algorithms with a large number of variables and datasets with optimal fitness, the use of multi-gene chromosomes is more effective. This is because each gene represents a small building block and contributes to the development of solutions for complex structures. These small building blocks are separate from each other and can therefore evolve independently.

In this study, model prediction was performed using GeneXproTools 5.0 software [44]. To obtain the optimum result, the process was repeated many times using a trial-and-error approach by adjusting the chromosome number, head and gene number, linkage model and the weights of the selected mathematical functions on the linkage. The optimal parameters selected for the GEP model are presented in Table 3. By summing the eight gene expression trees shown in Fig. 7, the following equation was derived for the axial load carrying capacity (N_u) of the CFST columns, which corresponds to the solution that gives the most accurate results.

$$N_u = N_1 + N_2 + N_3 + N_4 + N_5 + N_6 + N_7 + N_8 \tag{16}$$

$$N_1 = \frac{1}{\tan\left[\frac{1}{2f_c'} - \left((L - 14.959224) - (f_y - 17.769647)\right)\right]} \tag{16a}$$

$$N_2 = \left(3.07912L\sqrt{t_f}\right) - 2.296511\left(L + t_f\right) \tag{16b}$$

$$N_3 = \left(\left(E_f - 31.189813\right)t_f - L\right) + \left(Dt_s + f_c' - 14.274516\right) \tag{16c}$$

$$N_4 = \left(\frac{1}{D-L}\right)\left(-24.014124f_f\right) + \tan\left(f_y\right) \tag{16d}$$

$$N_5 = \left(\sin(f_c')t_s^3 + \tan\left(f_y\right)\right) + \tan\left(t_f + 13.835261\right) \tag{16e}$$

$$N_6 = \tan(78.709475f_c') + \tan\left(f_c'^2 + 4.073000\right) \tag{16f}$$

$$N_7 = \left(E_f^{1/4}(f_c' - 32.153456)\right)(t_s - 4.658426) - \tan\left(\sqrt{D}\right) \tag{16g}$$

$$N_8 = \left(\sqrt{L}(D + f_c')\right) - (11.644246D + L - 1) \tag{16h}$$

4.2 Multilayer perceptron

The Multilayer Perceptron (MLP) is similar to the learning process of the biological nervous system and each data is represented by neurons that are interrelated with each other. MLP consists of an input layer where the problem data is defined, hidden layers where the defined data is processed, and an output layer where classification or regression results are obtained according to the type of problem. Thanks to its feedforward algorithm, it minimizes errors in solving complex problems [45-46].

4.3 K-nearest neighbors

The K-Nearest Neighbors (KNN) is a supervised ML model that utilizes the distance between data points to perform regression or classification tasks. Before running the algorithm, the number of neighbors (K) is determined by selecting an initial distance value. If the value of K is small, a more precise and sensitive model are obtained in a short distance, whereas a larger K value results in a more generalized prediction by considering a broader range of data. During the prediction process, Argmax function is used to compute the average of the output values of the k-nearest neighbors within the dataset [47].

4.4 Bootstrap aggregating

Bagging (BAG), short for Bootstrap Aggregating, is an ML algorithm developed by combining subsets of randomly selected data from the original dataset. Each subset model is trained within itself, when making a prediction for new data, all subset predictions are averaged to generate the final result. This method prevents overfitting or memorization. The prediction value is computed using Eq. (17) below.

$$y_i = \frac{1}{B}\sum_{b=1}^{B} f_b(x_i) \tag{17}$$

where y_i represents the prediction result, B denotes the number of subsets obtained from the dataset, x_i signifies the data point to be predicted, b refers to the subset, and $f_b(x_i)$is the prediction function of the b^{th} subset [48].

4.5 Random forest

Random Forest (RF) is a supervised ML algorithm proposed by Breiman in 2001. It is called ‘random forest’ because it combines multiple algorithms of the same type to enhance predictive performance. It is a combination of the classification and regression tree (CART) algorithm [49]. While developing this model, two hyperparameters that are defined include decision tree depth and the number of decision trees. These hyperparameters are the main variables that determine the performance of RF [50]. The subset decision trees with randomly selected nodes are trained independently and make individual predictions. The algorithm iteratively makes predictions on the training data until an acceptable level of performance is reached. The final decision is obtained by averaging the predictions of the independent trees [45]. In Eq. (18), $f(x)$ represents the predicted output value, while $f_i(x)$ denotes the prediction function of the i^{th} tree, and n is the total number of decision trees in the ensemble.

$$f(x) = \frac{1}{n}\sum_{i=1}^{n} f_i\,(x) \tag{18}$$

4.6 Gradient boosting machine

Gradient Boosting Machine (GBM) is widely used algorithm for solving regression and classification problems. The algorithm, which follows the principle of training decision trees, begins by training a simple decision tree and generating initial predictions. In each iteration, new decision trees are incorporated to correct the errors of the existing model. The Gradient Descent method is used to minimize the errors in each iteration. This process continues until a predetermined number of trees is reached or until the model's errors become negligible and cannot be further reduced. However, using an excessive number of decision trees in large datasets increases the risk of overfitting [51].

4.7 Light gradient boosting machine

Light Gradient Boosting Machine (LightGBM) regression is a gradient boosting algorithm that predicts target variables using an ensemble of decision trees. Each tree is trained on the residuals of the model from the previous iteration to reduce the prediction error [52]. LightGBM provides faster and more efficient processing of each decision tree by using a histogram-based algorithm in the tree building process. Thanks to this feature, it provides an important advantage especially in large data sets. It implements a leaf-wise growth method with depth constraints in LightGBM. This approach enables faster determination of the optimum split points [53-54].

4.8 Extreme gradient boosting

Extreme Gradient Boosting (XGBoost) is a refined and enhanced version of the gradient boosting algorithm. It is highly effective in handling large datasets and solving complex problems [55-56]. The primary objective of the XGBoost model is to determine the optimal hyperparameters that minimize the discrepancy between actual values and predicted results. To improve the shortcomings of existing trees, it goes through a gradient boosting training where each tree is built sequentially and the results are merged along the path [46]. Unlike random forest, XGBoost constructs base models sequentially; the training of each weak learner depends on the performance of previous learners on the dataset [57]. A significant feature of XGBoost is its ability to handle missing data [48].

4.9 Categorical boosting

The categorical boosting (CatBoost) algorithm simplifies pre-processing and reduces potential errors by categorizing the data [58]. It uses a method called ‘ordered goal encoding technique’ in which variables take numerical values according to their goal statistics and their appearance in the datasets [59]. CatBoost uses dynamic lifting schemes to reduce overfitting. The algorithm performs well on classification and regression tasks for large datasets [45]. CatBoost arranges targets and outputs in a structured order, allowing the algorithm to understand their priority and relative importance. Unlike other gradient boosting (GB) algorithms, CatBoost operates using oblivious trees. In oblivious trees, only one feature is selected at a given level of a tree. The decision rules for splitting criteria are based solely on to this feature. In other boosting algorithms, weak learners are improved during each iteration, resulting in overfitting of the final learner. Due to the unknown trees, the chance of overfitting is low and the execution speed of the CatBoost model is also increased [60].

5. Model performance evaluation

5.1 Performance metrics

Table 4. Statistical metrics

Statistical criteria	Formulation
Mean absolute percentage error	$MAPE = \frac{100}{n}\sum_{i=1}^{n}\left\lvert\frac{exp_i - model_i}{exp_i}\right\rvert$
Root mean square error	$RMSE = \sqrt{\frac{\sum_{i=1}^{n}(exp_i - model_i)^2}{n}}$
Coefficient of determination	$R^2 = \frac{\left[\sum_{i=1}^{n}(exp_i - \overline{exp})(model_i - \overline{model})\right]^2}{\sum_{i=1}^{n}(exp_i - \overline{exp})^2 \sum_{i=1}^{n}(model_i - \overline{model})^2}$
Coefficient of variation	$COV = \frac{SD}{M} = \frac{\sqrt{\frac{\sum_{i=1}^{n}\left(\frac{exp_i}{model_i} - M\right)^2}{n-1}}}{\frac{1}{n}\sum_{i=1}^{n}\frac{exp_i}{model_i}}$

Table 5. Performance of machine learning and existing models on the training and testing datasets

Model	Training					Testing				
	Number of Data	$MAPE$	$RMSE$	R^2	COV	Number of Data	$MAPE$	$RMSE$	R^2	COV
Liu et al. [35]	144	18.861	666.710	0.909	0.176	48	17.837	681.917	0.900	0.219
Tang et al. [12]	137	24.748	851.459	0.821	0.227	45	24.885	962.747	0.830	0.327
Ding et al. [36]	137	13.778	601.674	0.883	0.184	45	15.146	716.594	0.873	0.217
Lu et al. [37]	161	13.599	478.803	0.911	0.180	54	14.243	524.819	0.917	0.195
Lu et al. [3]	170	14.685	521.065	0.906	0.190	57	15.683	567.071	0.909	0.203
Wei et al. [4]	144	14.885	555.705	0.901	0.185	48	15.135	625.542	0.894	0.207
Che et al. [1]	137	14.913	613.339	0.873	0.195	45	14.633	637.019	0.899	0.229
Tao et al. [10]	137	19.912	688.936	0.898	0.187	45	21.125	787.920	0.881	0.222
GEP	170	7.261	222.263	0.980	0.092	57	5.911	189.538	0.987	0.073
MLP	170	13.450	400.205	0.935	0.188	57	13.544	448.877	0.929	0.175
KNN	170	5.848	196.222	0.985	0.077	57	10.324	464.596	0.932	0.155
BAG	170	3.676	150.955	0.991	0.050	57	7.036	272.791	0.973	0.085
RF	170	3.589	149.183	0.991	0.049	57	7.405	282.557	0.971	0.088
GBM	170	2.926	108.093	0.995	0.039	57	5.251	200.915	0.986	0.078
LightGBM	170	4.418	143.815	0.992	0.061	57	7.101	227.283	0.982	0.101
XGBoost	170	2.333	112.491	0.995	0.034	57	5.405	222.201	0.984	0.108
CatBoost	170	1.950	96.664	0.996	0.030	57	4.075	180.509	0.988	0.059

The performance of all models will be statistically compared using metrics such as $MAPE$, $RMSE$, R^2 and COV. An R^2 value close to 1 indicates strong agreement between predictions and experimental data, while lower COV, $MAPE$ and $RMSE$ values indicate higher predictive accuracy. The statistical formulations of these metrics are summarized in Table 4.

5.2 Model comparison

In this study, the performance of different models was evaluated using 170 training and 57

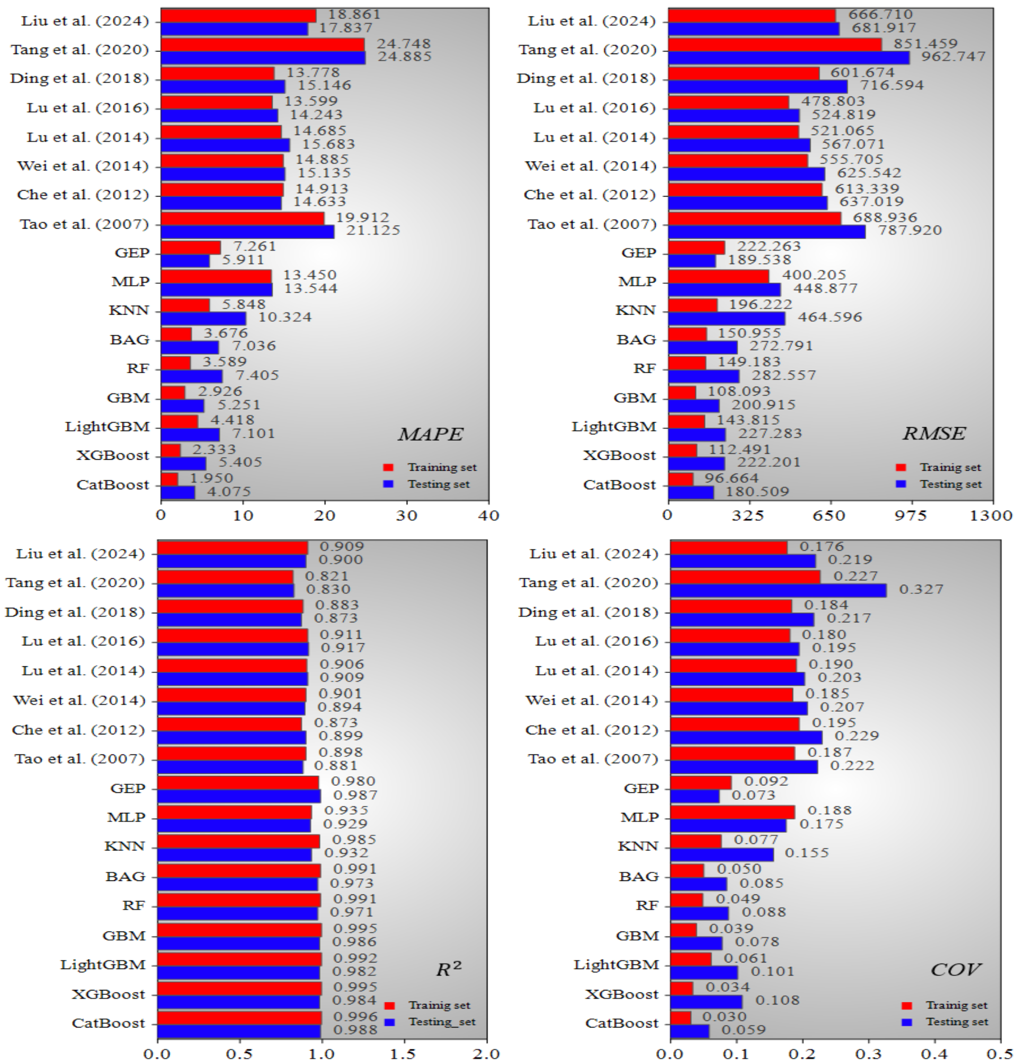

Figure 8. Statistical comparison of prediction results

testing data points compiled from the literature. A detailed comparison is presented in Table 5, and a visual representation is shown in Fig. 8. For empirical relationships developed under specific FRP types and boundary conditions, only experimental data meeting these conditions were included in the evaluation. Accordingly, the validity ranges and applicability conditions of existing models, including requirements such as FRP type, number of layers, and other parameter range constraints, were taken into account in the analysis. To ensure a fair and consistent comparison, Table 5 specifies the number of training and testing data points used within the applicability range for each empirical relationship. Due to the risk of overfitting, the comparison of the models is based on the results of the testing set, which better reflects actual performance, rather than the training test. The comparative analysis of various prediction models evaluated using $MAPE$, $RMSE$, R^2 and COV performance metrics is given in Table 5.

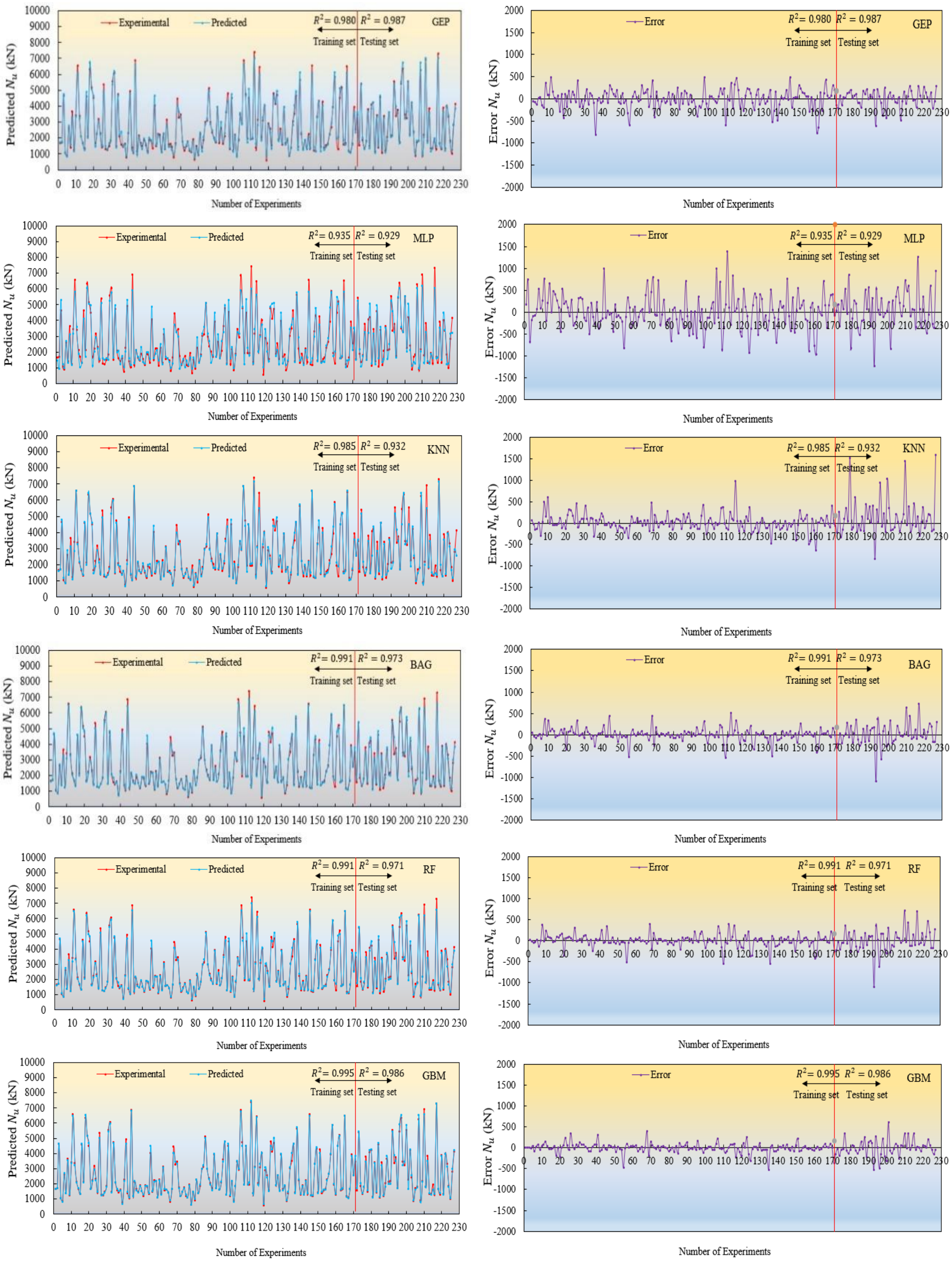

Figure 9. The comparisons of experimental results versus ML models

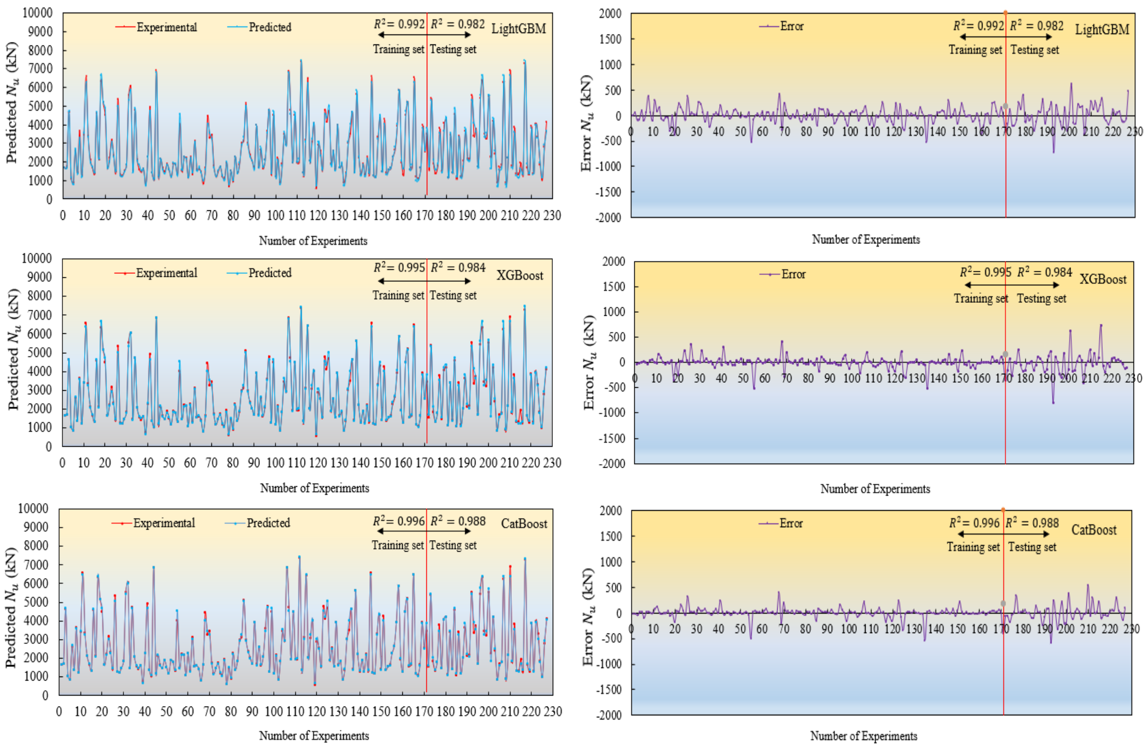

Figure 9. Continued

As can be seen in Table 5 and Fig. 8, advanced ML algorithms significantly outperformed traditional models in terms of accuracy, robustness and generalization. Among the traditional models, the Lu et al. [37] model demonstrated the best performance with the lowest $MAPE$ of 14.243, an $RMSE$ of 524.819, a COV of 0.195, and the highest R^2 value of 0.917. In contrast, the Tang et al. [12] model exhibited the worst performance, with the highest $MAPE$ of 24.885, an $RMSE$ of 962.747, a COV of 0.327, and the lowest R^2 of 0.830. CatBoost, one of the ML models reflecting both high accuracy and consistency, emerged as the most effective model, with the lowest $MAPE$ of 4.075, an $RMSE$ of 180.509, a COV of 0.059, and the highest R^2 value of 0.988. While the XGBoost and GBM algorithms provided high accuracy, with R^2 values of 0.984 and 0.986, respectively, they also yielded satisfactory results with low $MAPE$ values of 5.405 and 5.251. In addition, the BAG and RF models showed strong performance on the testing dataset. The BAG model achieved high accuracy with an R^2 value of 0.973, a $MAPE$ of 7.036, and an $RMSE$ of 272.791. Similarly, the RF algorithm also outperformed the traditional methods, achieving an R^2 value of 0.971, a $MAPE$ of 7.405, and an $RMSE$ of 282.557. The results reveal the inadequacy of traditional models in handling complex data structures and the superiority of ML algorithms in providing precise and reliable predictions across datasets.

In addition, Fig. 9 graphically shows the comparison of the prediction results obtained by ML algorithms with the experimental results. The error magnitudes are shown by using the red line for the experimental results and the blue line for the prediction results. As a result, CatBoost, GBM and GEP models demonstrated the best performance, achieving high accuracy on the testing set

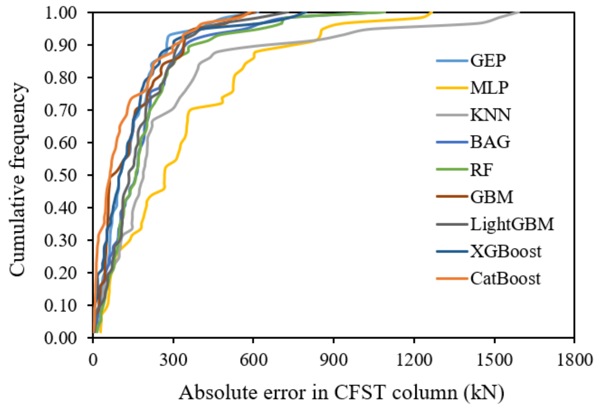

Figure 10. Cumulative frequency of absolute errors in ML prediction models for CFST columns

and low error distributions. XGBoost and RF models stand out especially with their balanced error distributions, while MLP and KNN models exhibited lower accuracy and generalization success compared to other models.

5.3 Error distribution analysis

In Fig. 10, the cumulative frequency diagram is presented to evaluate the performance of each ML model in predicting the axial load-carrying capacity of CFST columns. The 90% cumulative absolute error threshold is defined as the absolute error value below which 90% of the test predictions fall. For each model, the absolute errors between the experimental and predicted values were first calculated and then sorted in ascending order. The cumulative frequency was then obtained as the ratio of the number of predictions with absolute errors less than or equal to a given error value to the total number of test data. Therefore, this threshold was used to compare the error levels of the models at the same cumulative frequency level. A model is considered more accurate when the cumulative frequency curve rises rapidly at smaller error values, whereas a flatter curve at larger error values indicates lower predictive accuracy. As shown in Fig. 10, the GEP and CatBoost models exhibited the lowest error values with absolute errors of 276.49 and 296.88, respectively, corresponding to the 90% cumulative absolute accuracy threshold. The XGBoost and LightGBM models also performed well with slightly higher error values of 299.98 and 317.97. The GBM and BAG models performed moderately with error values of 338.07 and 342.73, while the RF model exhibited a higher error value of 360.28. The weakest performances were observed in the KNN and MLP models with error values of 603.5 and 721.64, respectively. As can be seen, other ML models except KNN and MLP showed superior performance in predicting the targets of CFST columns.

5.4 SHapley Additive exPlanations

SHapley Additive exPlanations (SHAP) is an interpretable ML method based on game theory proposed by Lundberg et al. [61]. The SHAP method is an emerging technique for quantifying the contributions of input parameters that influence the prediction results of a ML model. The magnitude of SHAP values reflects the contribution of each feature to the model predictions [61].

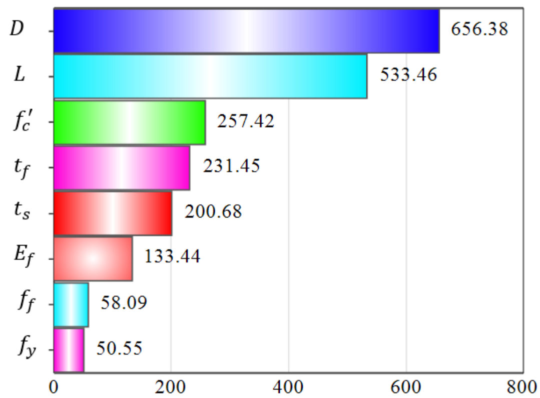

Figure 11. Feature importance based on mean absolute SHAP values

The model function $f(x)$ is given by the following Eq. (19):

$$f(x) = g(x') = \varphi_0 + \sum_{i=1}^{N} \varphi_i x_i'. \tag{19}$$

where N represents the number of input parameters, φ_0 is the base value, which corresponds to the model output when all input parameters are missing, φ_i denotes the attribution value of each input parameter. Lastly, x_i' is the simplified input parameter, expressed in scaled format [62]. The blue and red dots in Fig. 11 illustrate how the magnitude of the input parameters influences the model's predictions and indicate the direction of their impact. Blue dots represent lower values of the input parameter, while red dots represent higher values, following a color scale from low (blue) to high (red). In other words, positive SHAP values indicate that an increase in the input parameter leads to a higher prediction, while negative SHAP values suggest a decrease in the prediction. In this study, Shapley analysis was conducted for the CatBoost model due to its superior predictive performance compared to other ML models.

The feature importance of the input parameters is presented in Fig. 11 using the mean absolute SHAP values. It can be seen that D has the highest mean absolute SHAP value of the 656.38 among the parameters determining the performance of CFST columns. This result is consistent with structural mechanics, since the diameter determines the cross-sectional area and directly influences the load-carrying capacity. The (L) parameter is the second most important parameter, with a mean absolute SHAP value of 533.46. This result may be attributed to the influence of column length on slenderness-related behavior and buckling response, as well as the relatively wide variation of (L) values in the dataset. The effect of f_c' is moderate, with a value of 257.42, which is consistent with its role in determining the compressive strength of the concrete core and its contribution to the overall capacity of the column. t_f and t_s show lower importance, with values of 231.45 and 200.68. They do play a role in stiffness and confinement, but their influence is smaller compared to D and L. E_f has a relatively lower importance, with a value of 133.44. While it influences the stiffness of the section, its effect on the ultimate load capacity remains limited. f_f and f_y have the lowest SHAP values, 58.09 and 50.55, indicating that their influence on the overall structural behavior is quite limited under these conditions.

To further investigate the influence of each parameter, the SHAP summary plot is illustrated in Fig. 12. It is found that D, L and f_c' are the most important parameters for the column. The D has

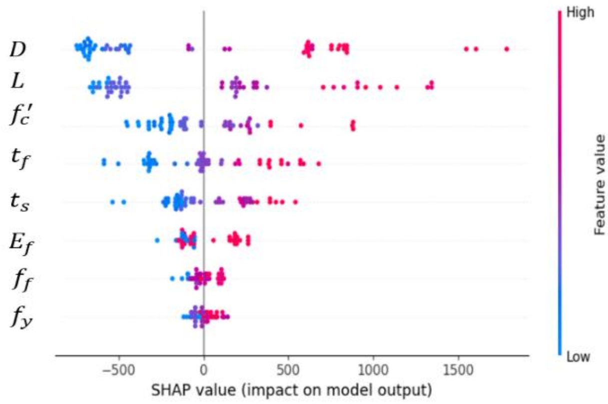

Figure 12. SHAP summary plot

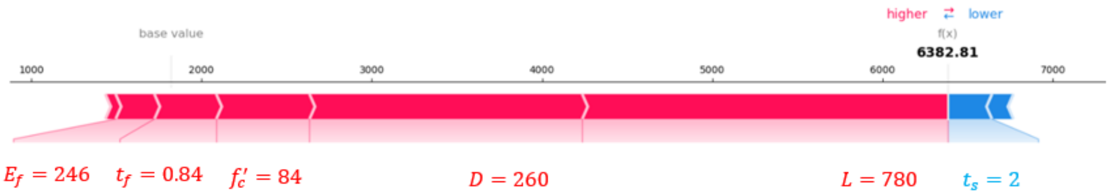

Figure 13. SHAP force plot for a specimen

the highest SHAP value and is the parameter that affects the model prediction the most. This shows that the D is an important role in the load carrying capacity of columns. When the SHAP values for the t_f and t_s were examined, it was observed that increases in these parameters mean an increasing trend for the load carrying capacity, but this increasing trend was less than the other parameters. Besides, the red and blue points of the E_f and f_f are mixed and limited compared to other variables. However, the f_y has the lowest impact on the model output among the other input parameters.

Finally, a SHAP force plot for a selected specimen from the testing dataset is presented in Fig. 13 to provide a local interpretability analysis. The value of the $f(x)$ in the SHAP force plot shows the predictive power of the model by adding or subtracting the contributions of each parameter to the base value. The length of each red and blue bar represents the higher and lower contributions of the parameters on the output predictions through the SHAP values. As shown in Fig. 13, L, D, f_c', t_f and E_f with red bars contribute positively to the prediction model, while the t_s with blue bar has a negatively effect.

The scatter plots and histogram distributions presented in Figs. 3 and 4 indicate that the dataset has an imbalanced structure, with some variables concentrated within specific ranges. This is due to the variables being tested at predetermined discrete levels in the experimental studies. Nevertheless, the high performance of the model can be explained by the regression-based nature of the problem, the presence of strong physical relationships among the input variables, and the model's ability to learn these relationships. SHAP analyses also indicate that the model does not rely solely on the dominant portion of the dataset for learning.

6. Conclusions

In this study, the performance of different models is evaluated using 170 training and 57 testing datasets collected from the literature. Gene Expression Programming (GEP) and various machine learning (ML) models were used to predict the axial load carrying capacity of CFST columns externally confined with fiber-reinforced polymer (FRP). The prediction results were then compared with experimental data and existing equations in the literature, and model performance was evaluated using statistical criteria based on the testing results to reduce the risk of overfitting. The findings of this study are summarized below:

- In comparison with the existing equations in the literature, machine learning models demonstrated more accurate predictions of the axial load-carrying capacity of columns. Their ability to capture complex relationships, process a larger number of variables, and reduce errors through model optimization significantly enhances their predictive performance compared with traditional regression models.
- When the prediction results of the existing equations and ML models were compared, the CatBoost model emerged as the most accurate, with a $MAPE$ of 4.075, an $RMSE$ of 180.509, an R^2 of 0.988, and a COV of 0.059. These findings demonstrate that CatBoost effectively captures the key variables influencing axial load-carrying capacity.
- Among the existing equations in the literature, the Lu et al. [37] model provided the most accurate predictions, with a $MAPE$ of 14.243, an $RMSE$ of 524.819, an R^2 of 0.917, and a COV of 0.195. In contrast, the Tang et al. [12] model had the least accuracy, with a $MAPE$ of 24.885, an $RMSE$ of 962.747, an R^2 of 0.830, and a COV of 0.327.
- In the results of the feature significance analysis for the CatBoost model, the diameter (D) and length (L) of the column show the highest SHAP values and emerge as the overriding parameters in estimating the axial load-carrying capacity. This highlights the dominant influence of column geometry on the load-carrying capacity. In addition, material properties such as concrete compressive strength (f_c'), steel tube wall thickness (t_f) and FRP layer thickness (t_s) were found to have a significant impact on the model. On the other hand, the effects of FRP elastic modulus (E_f), FRP strength (f_f) and steel yield strength (f_y) variables were found to be relatively less significant.
- This study has some limitations. The dataset is not fully balanced in terms of parameter ranges, column geometries, and FRP types, with some types such as CFRP being more dominant. In addition, the dataset mainly represents short columns; therefore, the buckling behavior of long and slender columns is only represented to a limited extent. Accordingly, the results should be evaluated within the scope and distribution of the dataset used. Future studies may consider larger and more balanced datasets, eccentric loading conditions, long columns, different FRP types, and hybrid ML models. Despite these limitations, the results confirm the potential of ML-based approaches for predicting the axial load-carrying capacity of FRP-confined CFST columns and provide a useful basis for developing more robust and generalizable prediction systems in future research.

References

1. Che, Y., Wang, Q.L., Shao, Y.B. (2012). Compressive performances of the concrete filled circular CFRP-steel tube (C-CFRP-CFST). Advances in Steel Construction, 8(4), 331-356.

2. Alwash, N.A., Al-Salih, H.I. (2013). Experimental investigation on behavior of SCC filled steel tubular stub columns strengthened with CFRP. Construction Engineering, 1(2), 37-51.
3. Lu, Y., Li, N., Li, S. (2014). Behavior of FRP-confined concrete-filled steel tube columns. Polymers, 6(5), 1333-1349. https://doi.org/10.3390/polym6051333.
4. Wei, Y., Wu, G., Li, G. (2014). Performance of circular concrete-filled fiber-reinforced polymer-steel composite tube columns under axial compression. Journal of Reinforced Plastics and Composites, 33(20), 1911-1928. https://doi.org/10.1177/0731684414550836.
5. Akkaya, H.C., Aydemir, C., Arslan, G. (2022). An experimental research on reinforced concrete deep beams fully wrapped with fiber reinforced polymers against shear. Case Studies in Construction Materials, 17, e01198. https://doi.org/10.1016/j.cscm.2022.e01198.
6. Akkaya, H.C., Aydemir, C., Arslan, G. (2022). Investigation on shear behavior of reinforced concrete deep beams without shear reinforcement strengthened with fiber reinforced polymers. Case Studies in Construction Materials, 17, e01392. https://doi.org/10.1016/j.cscm.2022.e01392.
7. Akkaya, H.C., Aydemir, C., Arslan, G. (2024). Evaluation of shear behavior of short-span reinforced concrete deep beams strengthened with fiber reinforced polymer strips. Engineering Structures, 299, 117145. https://doi.org/10.1016/j.engstruct.2023.117145.
8. Cakir, F., Aydin, M.R., Acar, V., Aksar, B., Akkaya, H.C. (2023). An experimental study on RC beams shear-strengthened with intraply hybrid U-jackets Composites monitored by digital image correlation (DIC). Composite Structures, 323, 117503. https://doi.org/10.1016/j.compstruct.2023.117503.
9. Xiao, Y., He, W., Choi, K.K. (2005). Confined concrete-filled tubular columns. Journal of Structural Engineering, 131(3), 488-497. https://doi.org/10.1061/(ASCE)0733-9445(2005)131:3(488).
10. Tao, Z., Han, L.H., Zhuang, J.P. (2007). Axial loading behavior of CFRP strengthened concrete-filled steel tubular stub columns. Advances in Structural Engineering, 10(1), 37-46. https://doi.org/10.1260/136943307780150814.
11. Li, N., Lu, Y., Li, S., Liu, L. (2018). Slenderness effects on concrete-filled steel tube columns confined with CFRP. Journal of Constructional Steel Research, 143, 110-118. https://doi.org/10.1016/j.jcsr.2017.12.014.
12. Tang, H., Chen, J., Fan, L., Sun, X., Peng, C. (2020). Experimental investigation of FRP-confined concrete-filled stainless steel tube stub columns under axial compression. Thin-Walled Structures, 146, 106483. https://doi.org/10.1016/j.tws.2019.106483.
13. Ma, Y., Ma, K., Han, X., Yao, T. (2023). Experimental investigation of FRP-confined HSC-filled steel tube stub columns under axial compression. Engineering Structures, 280, 115670. https://doi.org/10.1016/j.engstruct.2023.115670.
14. Hu, Y.M., Yu, T., Teng, J.G. (2011). FRP-confined circular concrete-filled thin steel tubes under axial compression. Journal of Composites for Construction, 15(5), 850-860. https://doi.org/10.1061/(ASCE)CC.1943-5614.0000217.
15. Ma, K., Wang, Q., Lin, G., Xing, G. (2024). Axial compression performance of high-temperature-exposed concrete-filled steel tubular columns repaired with carbon fiber reinforced polymer. Journal of Constructional Steel Research, 213, 108400. https://doi.org/10.1016/j.jcsr.2023.108400.
16. Akkaya, H.C., Alacalı, S. (2025). Developing a new model using gene expression programming on the prediction of moment capacity of ferrocement elements. Bitlis Eren Üniversitesi Fen Bilimleri Dergisi, 14(2), 713-731. https://doi.org/10.17798/bitlisfen.1583956.
17. Akkaya, H.C., Alacalı, S. (2026). Predicting the punching shear capacity of RC slab-column connections with FRP bars using machine learning based algorithms. Latin American Journal of Solids and Structures, 23(2), e8817. https://doi.org/10.1590/1679-7825/e8817.
18. Alacali, S., Arslan, G. (2024). A prediction model for plastic hinge length of rectangular RC columns using gene expression programming. Neural Computing and Applications, 36(16), 9481-9501. https://doi.org/10.1007/s00521-024-09578-1.
19. Alacali, S., Arslan, G. (2025). Assessment of shear strength of steel fiber reinforced concrete (SFRC) beams using gene expression programming. Computers and Concrete, 35(5), 537-555. https://doi.org/10.12989/cac.2025.35.5.537.

20. Aydogan, M.S., Alacali, S., Arslan, G. (2023). Prediction of moment redistribution capacity in reinforced concrete beams using gene expression programming. Structures, 47, 2209-2219. https://doi.org/10.1016/j.istruc.2022.12.054.
21. Alacali, S., Akkaya, H.C., Sengun, K., Arslan, G. (2024). Proposal and evaluation of new models for predicting the FRP contribution to shear strength in reinforced concrete beams using gene expression programming. Neural Computing and Applications, 36(25), 15515-15544. https://doi.org/10.1007/s00521-024-09892-8.
22. Ye, M., Li, L., Yoo, D.Y., Li, H., Zhou, C., Shao, X. (2023). Prediction of shear strength in UHPC beams using machine learning-based models and SHAP interpretation. Construction and Building Materials, 408, 133752. https://doi.org/10.1016/j.conbuildmat.2023.133752.
23. Almasabha, G., Al-Shboul, K.F., Shehadeh, A., Alshboul, O. (2023). Machine learning-based models for predicting the shear strength of synthetic fiber reinforced concrete beams without stirrups. Structures, 52, 299-311. https://doi.org/10.1016/j.istruc.2023.03.170.
24. Zareian, F., Banazadeh, M., Zareian, M.S. (2024). Prediction of nonlinear dynamic responses and generation of seismic fragility curves for steel moment frames using boosting machine learning techniques. Computers & Structures, 305, 107580. https://doi.org/10.1016/j.compstruc.2024.107580.
25. Güneyisi, E.M., Gültekin, A., Mermerdaş, K. (2016). Ultimate capacity prediction of axially loaded CFST short columns. International Journal of Steel Structures, 16(1), 99-114. https://doi.org/10.1007/s13296-016-3009-9.
26. Tran, V.L., Thai, D.K., Kim, S.E. (2019). A new empirical formula for prediction of the axial compression capacity of CCFT columns. Steel and Composite Structures, 33(2), 181-194. https://doi.org/10.12989/scs.2019.33.2.181.
27. Tran, V.L., Thai, D.K., Nguyen, D.D. (2020). Practical artificial neural network tool for predicting the axial compression capacity of circular concrete-filled steel tube columns with ultra-high-strength concrete. Thin-Walled Structures, 151, 106720. https://doi.org/10.1016/j.tws.2020.106720.
28. Zarringol, M., Thai, H.T., Thai, S., Patel, V. (2020). Application of ANN to the design of CFST columns. Structures, 28, 2203-2220. https://doi.org/10.1016/j.istruc.2020.10.048.
29. Vu, Q.V., Truong, V.H., Thai, H.T. (2021). Machine learning-based prediction of CFST columns using gradient tree boosting algorithm. Composite Structures, 259, 113505. https://doi.org/10.1016/j.compstruct.2020.113505.
30. Naser, M.Z., Thai, S., Thai, H.T. (2021). Evaluating structural response of concrete-filled steel tubular columns through machine learning. Journal of Building Engineering, 34, 101888. https://doi.org/10.1016/j.jobe.2020.101888.
31. Hou, C., Zhou, X.G. (2022). Strength prediction of circular CFST columns through advanced machine learning methods. Journal of Building Engineering, 51, 104289. https://doi.org/10.1016/j.jobe.2022.104289.
32. Güneyisi, E.M., Nour, A.I. (2019). Axial compression capacity of circular CFST columns transversely strengthened by FRP. Engineering Structures, 191, 417-431. https://doi.org/10.1016/j.engstruct.2019.04.056.
33. Miao, K., Pan, Z., Chen, A., Wei, Y., Zhang, Y. (2023). Machine learning-based model for the ultimate strength of circular concrete-filled fiber-reinforced polymer-steel composite tube columns. Construction and Building Materials, 394, 132134. https://doi.org/10.1016/j.conbuildmat.2023.132134.
34. Goode, C.D., Lam, D. (2011). Concrete-filled steel tube columns-tests compared with Eurocode 4. Composite Construction in Steel and Concrete VI, 317-325. https://doi.org/10.1061/41142(396)26.
35. Liu, J., Wei, Y., Liu, Z., Cui, Z. (2024). Effects of seawater corrosion on compression-induced buckling performance of FRP-CFST columns. Engineering Failure Analysis, 162, 108441. https://doi.org/10.1016/j.engfailanal.2024.108441.
36. Ding, F.X., Lu, D.R., Bai, Y., Gong, Y.Z., Yu, Z.W., Ni, M., Li, W. (2018). Behaviour of CFRP-confined concrete-filled circular steel tube stub columns under axial loading. Thin-Walled Structures, 125, 107-118. https://doi.org/10.1016/j.tws.2018.01.015.
37. Lu, Y.Y., Li, S., Li, N. (2016). Study on property of concentrically compressed concrete filled circular

FRP-steel tube stub columns. Journal of China Railway Society, 38(4), 105-111. https://doi.org/10.3969/j.issn.1001-8360.2016.04.015.
38. Han, L.H., Yao, G.H., Zhao, X.L. (2005). Tests and calculations for hollow structural steel (HSS) stub columns filled with self-consolidating concrete (SCC). Journal of Constructional Steel Research, 61(9), 1241-1269. https://doi.org/10.1016/j.jcsr.2005.01.004.
39. Sakino, K., Nakahara, H., Morino, S., Nishiyama, I. (2004). Behavior of centrally loaded concrete-filled steel-tube short columns. Journal of Structural Engineering, 130(2), 180-188. https://doi.org/10.1061/(ASCE)0733-9445(2004)130:2(180).
40. Han, L.H., Yao, G.H., Zhao, X.L. (2004). Behavior and calculation on concrete-filled steel CHS (Circular hollow section) beam-columns. Steel and Composite Structures, 4(3), 169-188. https://doi.org/10.12989/scs.2004.4.3.169.
41. Yu, Q. (2002). Behaviors of FRP-confined concrete columns. Ph.D. Dissertation, Harbin Institute of Technology, Harbin, China.
42. Ferreira, C. (2001). Gene expression programming: A new adaptive algorithm for solving problems. Complex Systems, 13(2), 87-129.
43. Ferreira, C. (2002). Gene expression programming in problem solving. Soft Computing and Industry. Springer, London, UK.
44. GeneXproTools (2023). GeneXproTools: Data modeling and analysis software. Gepsoft, Capelo, Portugal. https://www.gepsoft.com/.
45. Wang, X., Li, T., Wang, Y., Xu, Y. (2024). Postblast damage assessment of concrete-filled double-skin tube columns by intelligence-based techniques. Journal of Constructional Steel Research, 215, 108486. https://doi.org/10.1016/j.jcsr.2024.108486.
46. Xu, Y., Zheng, B., Zhang, M. (2021). Capacity prediction of cold-formed stainless steel tubular columns using machine learning methods. Journal of Constructional Steel Research, 182, 106682. https://doi.org/10.1016/j.jcsr.2021.106682.
47. Hong, Z.T., Wang, W.D., Zheng, L., Shi, Y.L. (2023). Machine learning models for predicting axial compressive capacity of circular CFDST columns. Structures, 57, 105285. https://doi.org/10.1016/j.istruc.2023.105285.
48. Bakır, R., Orak, C., Yüksel, A. (2024). Optimizing hydrogen evolution prediction: A unified approach using random forests, LightGBM, and Bagging Regressor ensemble model. International Journal of Hydrogen Energy, 67, 101-110. https://doi.org/10.1016/j.ijhydene.2024.04.173.
49. Zhang, D., Chen, Y., Zhang, C., Xue, G., Zhang, J., Zhang, M., Wang, L., Li, N. (2023). Prediction of seismic acceleration response of precast segmental self-centering concrete filled steel tube single-span bridges based on machine learning method. Engineering Structures, 279, 115574. https://doi.org/10.1016/j.engstruct.2022.115574.
50. Zhang, B., Xue, X. (2024). Ultimate axial strength prediction of concrete-filled double-skin steel tube columns using soft computing methods. Engineering Applications of Artificial Intelligence, 129, 107676. https://doi.org/10.1016/j.engappai.2023.107676.
51. Yang, P.B., Chan, Y.J., Yazdi, S.K., Lim, J.W. (2024). Optimisation and economic analysis of industrial-scale anaerobic co-digestion (ACoD) of palm oil mill effluent (POME) and decanter cake (DC) using machine learning models: A comparative study of Gradient Boosting Machines (GBM), K-nearest neighbours (KNN), and random forest (RF). Journal of Water Process Engineering, 58, 104752. https://doi.org/10.1016/j.jwpe.2023.104752.
52. Wang, M., Mitri, H.S., Zhao, G., Wu, J., Xu, Y., Liang, W., Wang, N. (2024). Performance comparison of several explainable hybrid ensemble models for predicting carbonation depth in fly ash concrete. Journal of Building Engineering, 98, 111246. https://doi.org/10.1016/j.jobe.2024.111246.
53. Sheng, K., Jiang, G., Du, M., He, Y., Dong, T., Yang, L. (2024). Interpretable knowledge-guided framework for modeling reservoir water-sensitivity damage based on Light Gradient Boosting Machine using Bayesian optimization and hybrid feature mining. Engineering Applications of Artificial Intelligence, 133, 108511. https://doi.org/10.1016/j.engappai.2024.108511.
54. Song, X., Chen, Z.S. (2024). Enhancing financial time series forecasting in the shipping market: A

hybrid approach with Light Gradient Boosting Machine. Engineering Applications of Artificial Intelligence, 136, 108942. https://doi.org/10.1016/j.engappai.2024.108942.
55. Hernandez Obando, M.D.C., Iqbal, M., Zhang, D., Zhang, P.F., Zhao, Q. (2024). Axial strength prediction of seawater sea sand concrete-filled circular FRP tubes under alkaline environment based on ensemble learning algorithms. Thin-Walled Structures, 195, 111530. https://doi.org/10.1016/j.tws.2023.111530.
56. Lai, D., Demartino, C., Xiao, Y. (2024). Probabilistic machine learning models for predicting the maximum displacements of concrete-filled steel tubular columns subjected to lateral impact loading. Engineering Applications of Artificial Intelligence, 135, 108704. https://doi.org/10.1016/j.engappai.2024.108704.
57. Xu, Y., Zhang, M., Zheng, B. (2021). Design of cold-formed stainless steel circular hollow section columns using machine learning methods. Structures, 33, 2755-2770. https://doi.org/10.1016/j.istruc.2021.06.030.
58. Taherdangkoo, R., Nagel, T., Chen, C., Mollaali, M., Ghasabeh, M., Cuisinier, O., Abdallah, A., Butscher, C. (2024). Modeling unsaturated hydraulic conductivity of compacted bentonite using a constrained CatBoost with bootstrap analysis. Applied Clay Science, 260, 107530. https://doi.org/10.1016/j.clay.2024.107530.
59. Ghorbani, E., Yagiz, S. (2024). Estimating the penetration rate of tunnel boring machines via gradient boosting algorithms. Engineering Applications of Artificial Intelligence, 136, 108985. https://doi.org/10.1016/j.engappai.2024.108985.
60. Ahmed, U., Khan, A.R., Mahmood, A., Rafiq, I., Ghannam, R., Zoha, A. (2024). Short-term global horizontal irradiance forecasting using weather classified categorical boosting. Applied Soft Computing, 155, 111441. https://doi.org/10.1016/j.asoc.2024.111441.
61. Lundberg, S.M., Lee, S.I. (2017). A unified approach to interpreting model predictions. Advances in neural information processing systems 30 (NIPS 2017), Long Beach, CA, USA, December.
62. Jayasinghe, T., Chen, B.W., Zhang, Z., Meng, X., Li, Y., Gunawardena, T., Mangalathu, S., Mendis, P. (2023). Data-driven shear strength predictions of recycled aggregate concrete beams with/without shear reinforcement by applying machine learning approaches. Construction and Building Materials, 387, 131604. https://doi.org/10.1016/j.conbuildmat.2023.131604.
63. Hu, Q., Liu, C., Wang, Y., Zhang, S., Yu, T. (2022). Experimental investigations of FRP-interlayer-steel confined concrete columns under axial compression. Structures, 43, 1002-1017. https://doi.org/10.1016/j.istruc.2022.07.021.
64. Ma, L., Zhou, C., Lee, D., Zhang, J. (2022). Prediction of axial compressive capacity of CFRP-confined concrete-filled steel tubular short columns based on XGBoost algorithm. Engineering Structures, 260, 114239. https://doi.org/10.1016/j.engstruct.2022.114239.
65. Chen, Z., Pang, Y., Xu, R., Zhou, J., Xu, W. (2022). Mechanical performance of ocean concrete-filled circular CFRP-steel tube columns under axial compression. Journal of Constructional Steel Research, 198, 107514. https://doi.org/10.1016/j.jcsr.2022.107514.
66. Zeng, J.J., Zheng, Y.W., Liu, F., Guo, Y.C., Hou, C. (2021). Behavior of FRP ring-confined CFST columns under axial compression. Composite Structures, 257, 113166. https://doi.org/10.1016/j.compstruct.2020.113166.
67. Wei, Y., Zhang, Y., Chai, J., Wu, G., Dong, Z. (2020). Experimental investigation of rectangular concrete-filled fiber reinforced polymer (FRP)-steel composite tube columns for various corner radii. Composite Structures, 244, 112311. https://doi.org/10.1016/j.compstruct.2020.112311.
68. Cao, S., Wu, C., Wang, W. (2020). Behavior of FRP confined UHPFRC-filled steel tube columns under axial compressive loading. Journal of Building Engineering, 32, 101511. https://doi.org/10.1016/j.jobe.2020.101511.
69. Zhao, J., Xu, C., Sun, L., Wu, D. (2020). Behaviour of FRP-confined compound concrete-filled circular thin steel tubes under axial compression. Advances in Structural Engineering, 23(9), 1772-1784. https://doi.org/10.1177/1369433219900941.
70. Liu, J., Xu, T., Guo, Y., Wang, X., Chen, Y.F. (2019). Behavior of circular CFRP-steel composite tubed

high-strength concrete columns under axial compression. Composite Structures, 211, 596-609. https://doi.org/10.1016/j.compstruct.2019.01.011.
71. Liu, J.P., Xu, T.X., Wang, Y.H., Guo, Y. (2018). Axial behaviour of circular steel tubed concrete stub columns confined by CFRP materials. Construction and Building Materials, 168, 221-231. https://doi.org/10.1016/j.conbuildmat.2018.02.131.
72. Cao, Q., Tao, J., Wu, Z., Ma, Z.J. (2017). Behavior of FRP-steel confined concrete tubular columns made of expansive self-consolidating concrete under axial compression. Journal of Composites for Construction, 21(5), 04017040. https://doi.org/10.1061/(ASCE)CC.1943-5614.0000818.
73. Deng, J., Zheng, Y., Wang, Y., Liu, T., Li, H. (2017). Study on axial compressive capacity of FRP-confined concrete-filled steel tubes and its comparisons with other composite structural systems. International Journal of Polymer Science, 2017, 6272754. https://doi.org/10.1155/2017/6272754.
74. Yu, T., Hu, Y.M., Teng, J.G. (2014). FRP-confined circular concrete-filled steel tubular columns under cyclic axial compression. Journal of Constructional Steel Research, 94, 33-48. https://doi.org/10.1016/j.jcsr.2013.11.003.
75. Park, J.W., Hong, Y.K., Hong, G.S., Kim, J.H., Choi, S.M. (2011). Design formulas of concrete filled circular steel tubes reinforced by carbon fiber reinforced plastic sheets. Procedia Engineering, 14, 2916-2922. https://doi.org/10.1016/j.proeng.2011.07.367.
76. Liu, L., Lu, Y. (2010). Axial bearing capacity of short FRP confined concrete-filled steel tubular columns. Journal of Wuhan University of Technology-Materials Science Edition, 25(3), 454-458. https://doi.org/10.1007/s11595-010-0022-2.
77. Wang, Q.L., Wang, J.Y., Zhang, Y.D. (2006). Mechanical property analysis on axially compressed concrete filled circular CFRP-steel tube stub columns. Engineering Mechanics, 23(8), 102-105.

Appendix

Table A1. Summary of variables in the dataset

Research	FRP Type	D (mm)	t_s (mm)	t_f (mm)	f_f (MPa)	E_f (GPa)	L (mm)	f_y (MPa)	f_c' (MPa)	N_u (kN)
[13]	CFRP	100	2.5	0.167	3961	240	200	286	51.28	1413
		100	2.5	0.334	3961	240	200	286	51.28	1661
		100	2.5	0.501	3961	240	200	286	51.28	1803
		100	3.5	0.167	3961	240	200	286	51.28	1572
		100	3.5	0.334	3961	240	200	286	51.28	1831
		100	3.5	0.501	3961	240	200	286	51.28	2032
		100	2.5	0.167	3961	240	200	286	67.44	1505
		100	2.5	0.334	3961	240	200	286	67.44	1731
		100	2.5	0.501	3961	240	200	286	67.44	1899
		100	3.5	0.167	3961	240	200	286	67.44	1621
		100	3.5	0.334	3961	240	200	286	67.44	1890
		100	3.5	0.501	3961	240	200	286	67.44	2130
	GFRP	100	2.5	0.170	2200	100	200	286	51.28	1202
		100	2.5	0.340	2200	100	200	286	51.28	1344
		100	2.5	0.510	2200	100	200	286	51.28	1479
		100	3.5	0.17	2200	100	200	286	51.28	1315
		100	3.5	0.34	2200	100	200	286	51.28	1506
		100	3.5	0.51	2200	100	200	286	51.28	1619
		100	2.5	0.17	2200	100	200	286	67.44	1338
		100	2.5	0.34	2200	100	200	286	67.44	1402
		100	2.5	0.51	2200	100	200	286	67.44	1496
		100	3.5	0.17	2200	100	200	286	67.44	1504
		100	3.5	0.34	2200	100	200	286	67.44	1580
		100	3.5	0.51	2200	100	200	286	67.44	1694
[63]	GFRP	165.1	3.5	3	1235	48	540	366	55.8	3959
		165.1	3.5	3	1235	48	540	366	55.8	4001
		165.1	3.5	3	1235	48	540	366	55.8	3950
		200.1	3	3	894	39.8	540	325	62.7	5175
		200.1	3	3	894	39.8	540	325	62.7	5198
[64]	CFRP	114	2	0.166	3425	232	400	236.9	41.4	1069
		114	2	0.332	3425	232	400	236.9	41.4	1331
		114	2	0.166	3425	232	400	236.9	21.32	886
		114	2	0.166	3425	232	400	236.9	42.984	1143
		114	2	0.332	3425	232	400	236.9	42.984	1429
		114	2	0.166	3425	232	400	236.9	31.904	930
		114	2	0.332	3425	232	400	236.9	31.904	1243

Table A1. Continued

Research	FRP Type	D (mm)	t_s (mm)	t_f (mm)	f_f (MPa)	E_f (GPa)	L (mm)	f_y (MPa)	f_c' (MPa)	N_u (kN)
[64]	CFRP	114	2	0.166	3425	232	400	236.9	21.072	850
		114	2	0.166	3425	232	400	236.9	14.328	654
		114	2	0.332	3425	232	400	236.9	14.328	799
		114	2	0.166	3425	232	400	236.9	24.008	899
		114	2	0.332	3425	232	400	236.9	24.008	1219
[65]	CFRP	152	5	0.167	3667.5	240	600	369	32.24	2203
		152	5	0.167	3667.5	240	600	369	32.24	2144
		152	5	0.167	3667.5	240	600	369	32.24	2241
		152	5	0.334	3667.5	240	600	369	32.24	2413
		152	5	0.334	3667.5	240	600	369	32.24	2567
		152	5	0.334	3667.5	240	600	369	32.24	2551
[66]	CFRP	219	6	0.334	4324.2	233	600	353.49	33.976	4151
		219	6	0.334	4324.2	233	600	353.49	33.976	4076
	PETFRP	219	6	1.682	770	19	600	353.49	33.976	4618
		219	6	1.682	770	19	600	353.49	33.976	4640
[67]	BFRP	133	3	0.111	2370	91.4	400	364.9	31.2	1179
		133	3	0.222	2370	91.4	400	364.9	31.2	1391
	CFRP	133	3	0.111	4067	239.8	400	364.9	31.2	1451
		133	3	0.222	4067	239.8	400	364.9	31.2	1555
[12]	CFRP	114.5	3.02	0.167	3418	243	402	355	24.8	891
		114.6	3.04	0.167	3418	243	402.5	355	24.8	872
		114.6	3.07	0.334	3418	243	402.5	355	24.8	1044
		114.5	3.05	0.334	3418	243	402	355	24.8	1118
		114.8	3.02	0.501	3418	243	402.5	355	24.8	1324
		114.6	3.02	0.501	3418	243	402	355	24.8	1283
		113.8	4.98	0.167	3418	243	402.5	340	24.8	1096
		113.9	5.02	0.167	3418	243	402	340	24.8	1121
		113.8	5.02	0.334	3418	243	402	340	24.8	1252
		113.8	4.99	0.334	3418	243	402.5	340	24.8	1198
		113.8	5.04	0.501	3418	243	402	340	24.8	1447
		113.8	5.02	0.501	3418	243	402	340	24.8	1469
		113.6	6.82	0.167	3418	243	402.5	279	24.8	1218
		113.6	6.86	0.167	3418	243	402.5	279	24.8	1183
		114	6.76	0.334	3418	243	402.5	279	24.8	1358
		113.9	6.84	0.334	3418	243	402	279	24.8	1311
		113.7	6.86	0.501	3418	243	403	279	24.8	1621
		113.8	6.78	0.501	3418	243	402.5	279	24.8	1659

Table A1. Continued

Research	FRP Type	D (mm)	t_s (mm)	t_f (mm)	f_f (MPa)	E_f (GPa)	L (mm)	f_y (MPa)	f_c' (MPa)	N_u (kN)
[68]	CFRP	133	4	0.334	2471	210	400	340	112.24	2628
		133	4	0.668	2471	210	400	340	112.24	3342
	GFRP	133	4	0.338	1582	79	400	340	112.24	2662
		133	4	0.676	1582	79	400	340	112.24	3646
[69]	CFRP	255	2.54	0.15	4050	257	510	272.7	45.04	3406
		255	2.54	0.15	4050	257	510	272.7	45.04	3484
		255	2.54	0.15	4050	257	510	272.7	45.04	3121
		255	2.54	0.15	4050	257	510	272.7	45.04	3398
		255	2.54	0.3	4050	257	510	272.7	45.04	4030
		255	2.54	0.3	4050	257	510	272.7	45.04	4453
		255	2.54	0.3	4050	257	510	272.7	45.04	3516
		255	2.54	0.3	4050	257	510	272.7	45.04	4275
		254	1.37	0.15	4050	257	510	302.5	43.44	3153
		254	1.37	0.15	4050	257	510	302.5	43.44	3133
		254	1.37	0.15	4050	257	510	302.5	43.44	2894
		254	1.37	0.15	4050	257	510	302.5	43.44	3033
		254	1.37	0.3	4050	257	510	302.5	43.44	3913
		254	1.37	0.3	4050	257	510	302.5	43.44	3948
		254	1.37	0.3	4050	257	510	302.5	43.44	3482
		254	1.37	0.3	4050	257	510	302.5	43.44	3639
		255	2.25	0.15	4050	257	510	284	28.32	2821
		255	2.25	0.15	4050	257	510	284	28.32	3002
		255	2.25	0.15	4050	257	510	284	28.32	3011
		255	2.25	0.15	4050	257	510	284	28.32	2928
		255	2.25	0.3	4050	257	510	284	28.32	3625
		255	2.25	0.3	4050	257	510	284	28.32	3250
		255	2.25	0.3	4050	257	510	284	28.32	3269
		255	2.25	0.3	4050	257	510	284	28.32	3805
[70]	CFRP	260	2	0.334	3512	246	780	299	58	4494
		260	2	0.334	3512	246	780	299	58	4747
		260	2	0.334	3512	246	780	299	58	4581
		260	2	0.668	3512	246	780	299	58	5567
		260	2	0.668	3512	246	780	299	58	5419
		260	2	0.668	3512	246	780	299	58	5558
		260	2	0.334	3512	246	600	299	84	4127
		260	2	0.334	3512	246	600	299	84	4230
		260	2	0.334	3512	246	600	299	84	4212
		260	2	0.668	3512	246	600	299	84	4523

Table A1. Continued

Research	FRP Type	D (mm)	t_s (mm)	t_f (mm)	f_f (MPa)	E_f (GPa)	L (mm)	f_y (MPa)	f'_c (MPa)	N_u (kN)
[70]	CFRP	260	2	0.668	3512	246	600	299	84	4939
		260	2	0.668	3512	246	600	299	84	4642
		260	2	0.334	3512	246	780	299	84	6567
		260	2	0.334	3512	246	780	299	84	6568
		260	2	0.334	3512	246	780	299	84	6514
		260	2	0.668	3512	246	780	299	84	6269
		260	2	0.668	3512	246	780	299	84	6332
		260	2	0.668	3512	246	780	299	84	6374
		260	2	0.835	3512	246	780	299	84	6927
[71]	CFRP	200	2	0.334	3400	235	600	264.3	45.68	2607
		200	2	0.668	3400	235	600	264.3	45.68	3456
		200	2	0.668	3400	235	600	264.3	45.68	3083
		200	2	0.668	3400	235	600	264.3	45.68	3327
		200	2	0.334	3400	235	600	264.3	53.44	3190
		200	2	0.668	3400	235	600	264.3	53.44	3846
		200	2	0.668	3400	235	600	264.3	53.44	3469
		200	2	0.668	3400	235	600	264.3	53.44	3776
		260	2	0.334	3400	235	780	264.3	45.68	3360
		260	2	0.668	3400	235	780	264.3	45.68	4780
		260	2	0.668	3400	235	780	264.3	45.68	4050
		260	2	0.668	3400	235	780	264.3	45.68	4757
		260	2	0.334	3400	235	780	264.3	53.44	4321
		260	2	0.668	3400	235	780	264.3	53.44	4711
		260	2	0.668	3400	235	780	264.3	53.44	5374
		260	2	0.668	3400	235	780	264.3	53.44	5131
[36]	CFRP	299	3.75	0.167	3481	245	900	311	31.44	4498
		305	3.77	0.167	3481	245	898	311	31.44	4504
		300	3.67	0.334	3481	245	898	311	31.44	5540
		299	3.7	0.334	3481	245	899	311	31.44	5438
		299	3.86	0.501	3481	245	899	311	31.44	6469
		300	3.71	0.167	3481	245	900	311	45.92	5647
		300	3.73	0.167	3481	245	899	311	45.92	5859
		300	3.87	0.167	3481	245	899	311	45.92	6067
		299	3.74	0.334	3481	245	900	311	45.92	6877
		300	3.68	0.334	3481	245	898	311	45.92	6888
		299	3.7	0.501	3481	245	899	311	45.92	7407
		300	3.71	0.501	3481	245	898	311	45.92	7309

Table A1. Continued

Research	FRP Type	D (mm)	t_s (mm)	t_f (mm)	f_f (MPa)	E_f (GPa)	L (mm)	f_y (MPa)	f_c' (MPa)	N_u (kN)
[72]	CFRP	150	3.5	0.334	3400	224	300	316	32	1712
		150	3.5	0.334	3400	224	300	316	32	1757
		150	3.5	0.334	3400	224	300	316	26	1752
		150	3.5	0.334	3400	224	300	316	26	1681
[73]	CFRP	165	2	0.334	2878	244	500	275	24.96	1949
[74]	GFRP	204	2	0.540	1825	80	400	226	45.6	1593
		202	1	0.680	1825	80	400	231	37.1	1283
[4]	BFRP	133	3	0.111	2370	91.4	400	364.9	24.96	1179
		133	3	0.222	2370	91.4	400	364.9	24.96	1391
		133	4.5	0.111	2370	91.4	400	364.9	27.76	1689
		133	4.5	0.222	2370	91.4	400	364.9	27.76	1934
		133	6	0.111	2370	91.4	400	364.9	27.76	2041
		133	6	0.222	2370	91.4	400	364.9	27.76	2190
		133	7.5	0.111	2370	91.4	400	364.9	27.76	2169
		133	7.5	0.222	2370	91.4	400	364.9	27.76	2265
	CFRP	133	3	0.111	4067	239.8	400	364.9	24.96	1451
		133	3	0.222	4067	239.8	400	364.9	24.96	1555
		133	4.5	0.111	4067	239.8	400	364.9	27.76	1806
		133	4.5	0.222	4067	239.8	400	364.9	27.76	1963
		133	6	0.111	4067	239.8	400	364.9	27.76	1876
		133	6	0.222	4067	239.8	400	364.9	27.76	2312
		133	7.5	0.111	4067	239.8	400	364.9	27.76	2091
		133	7.5	0.222	4067	239.8	400	364.9	27.76	2363
[2]	CFRP	100	2	0.131	4300	234	300	335	23.5	591
		100	2	0.131	4300	234	300	335	23.5	760
[1]	CFRP	127	1.5	0.167	4500	228	381	330	43.2	1018
		129	2.5	0.167	4500	228	387	330	43.2	1186
		131	3.5	0.167	4500	228	393	330	43.2	1406
		133	4.5	0.167	4500	228	399	330	43.2	1559
		136	6	0.167	4500	228	408	330	43.2	1891
		127	1.5	0.334	4500	228	381	330	43.2	1228
		129	2.5	0.334	4500	228	387	330	43.2	1384
		131	3.5	0.334	4500	228	393	330	43.2	1714
		133	4.5	0.334	4500	228	399	330	43.2	1865
		136	6	0.334	4500	228	408	330	43.2	2105
[14]	GFRP	204	2	0.17	1825.5	80.1	400	226	42	1878
		204	2	0.34	1825.5	80.1	400	226	42	2127

Table A1. Continued

Research	FRP Type	D (mm)	t_s (mm)	t_f (mm)	f_f (MPa)	E_f (GPa)	L (mm)	f_y (MPa)	f_c' (MPa)	N_u (kN)
[14]	GFRP	204	2	0.51	1825.5	80.1	400	226	42	2231
		203	1.5	0.34	1825.5	80.1	400	242	42	1950
		203	1.5	0.51	1825.5	80.1	400	242	42	2244
		203	1.5	0.68	1825.5	80.1	400	242	42	2561
		202	1	0.34	1825.5	80.1	400	231	36	1710
		202	1	0.51	1825.5	80.1	400	231	36	1961
		202	1	0.68	1825.5	80.1	400	231	36	2265
[75]	CFRP	139.8	3.2	0.11	3500	235	620	365	37.5	1409
		139.8	3.2	0.33	3500	235	620	365	37.5	2063
		139.8	4.5	0.11	3500	235	620	334	37.5	1653
		139.8	4.5	0.22	3500	235	620	334	37.5	1840
		139.8	4.5	0.33	3500	235	620	334	37.5	2139
		139.8	6.6	0.11	3500	235	620	301	37.5	1834
		139.8	6.6	0.33	3500	235	620	301	37.5	2275
[76]	CFRP	128	4	0.111	3550	250	400	248	35.92	1300
		128	4	0.222	3550	250	400	248	35.92	1440
		128	4	0.333	3550	250	400	248	35.92	1685
		126	3	0.222	3550	250	400	243	35.92	1330
		130	5	0.222	3550	250	400	242	35.92	1650
		128	4	0.222	3550	250	400	248	43.36	1548
		128	4	0.222	3550	250	400	248	48	1658
	GFRP	128	4	0.169	2930	109	400	248	35.92	1355
		128	4	0.338	2930	109	400	248	35.92	1693
		128	4	0.507	2930	109	400	248	35.92	1845
[10]	CFRP	156	3	0.17	4212	255	470	230	46	1890
		156	3	0.34	4212	255	470	230	46	2270
		250	3	0.17	4212	255	750	230	46	3940
		250	3	0.34	4212	255	750	230	46	4780
[77]	CFRP	127	1.5	0.167	4900	230	400	350	44	1086
		129	2.5	0.167	4900	230	400	350	44	1294
		131	3.5	0.167	4900	230	400	310	44	1348
		133	4.5	0.167	4900	230	400	310	44	1698
		136	6	0.167	4900	230	400	350	42.4	1939
		127	1.5	0.334	4900	230	400	350	44	1283
		129	2.5	0.334	4900	230	400	350	44	1506
		131	3.5	0.334	4900	230	400	310	44	1593
		133	4.5	0.334	4900	230	400	310	44	1846
		136	6	0.334	4900	230	400	350	42.4	2186

Table A1. Continued

Research	FRP Type	D (mm)	t_s (mm)	t_f (mm)	f_f (MPa)	E_f (GPa)	L (mm)	f_y (MPa)	f_c' (MPa)	N_u (kN)
[9]	CFRP	152	2.95	0.28	897	64.9	1500	356	46.6	2233
		152	2.95	0.28	897	64.9	1500	356	46.6	2266
		152	2.95	0.56	897	64.9	1500	356	46.6	3439
		152	2.95	0.56	897	64.9	1500	356	46.6	3438